Cell Stem Cell

Article

Kupffer-cell-derived IL-6 is repurposed for hepatocyte dedifferentiation via activating progenitor genes from injury-specific enhancers

Graphical abstract

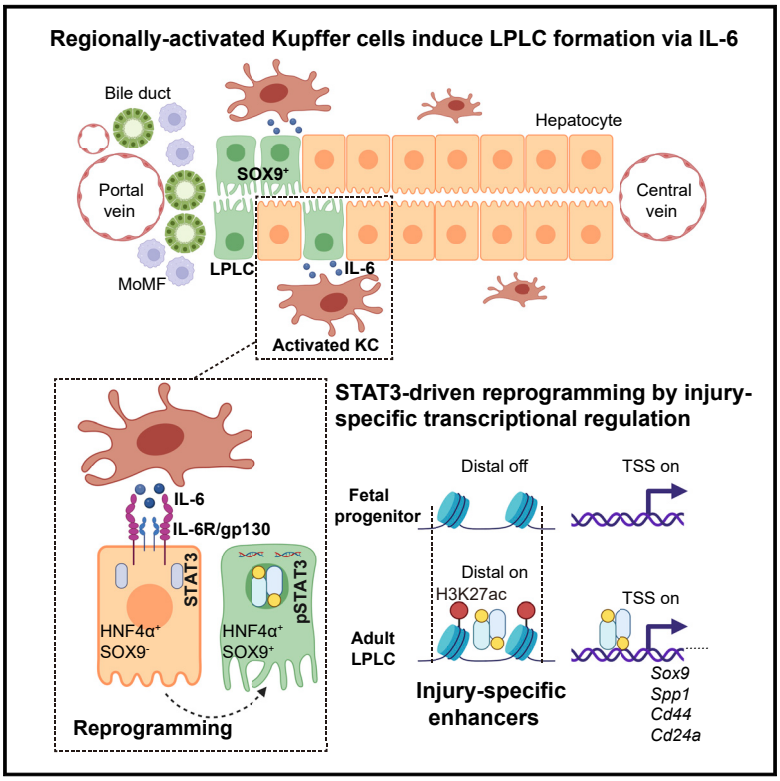

Highlights

- Single-cell atlas of hepatocyte dynamics following periportal liver injury
- Hepatocyte dedifferentiation is induced by regionally activated Kupffer cells
- Kupffer-cell-derived IL-6 is repurposed for hepatocyte dedifferentiation
- STAT3 activates reprogramming/progenitor-related genes via injury-specific enhancers

Authors

Lu Li, Lei Cui, Ping Lin, ..., Yixue Li, Hong Li, Lijian Hui

Correspondence

yxli@sibs.ac.cn (Y.L.), lihong01@sibs.ac.cn (H.L.), ljhui@sibcb.ac.cn (L.H.)

In brief

Hui and colleagues delineate the transcriptional dynamics of hepatocyte responses to liver injury and report that the proinflammatory factor IL-6 from Kupffer cells is repurposed for hepatocyte dedifferentiation. Activated IL-6/STAT3 signaling drives the expression of reprogramming/progenitor-related genes through injury-specific rather than embryogenesis-related enhancers.

Li et al., 2023, Cell Stem Cell *30*, 1–17
March 2, 2023
https://doi.org/10.1016/j.stem.2023.01.009

CellPress

Cell Stem Cell

CellPress

Article

Kupffer-cell-derived IL-6 is repurposed for hepatocyte dedifferentiation via activating progenitor genes from injury-specific enhancers

Lu Li,[1,15] Lei Cui,[1,15] Ping Lin,[2,15] Zhaoyuan Liu,[3] Shujie Bao,[1] Xiaolong Ma,[1] Haitao Nan,[1] Wencheng Zhu,[1] Jin Cen,[1] Yunuo Mao,[4] Xiong Ma,[5] Lingyong Jiang,[6] Yu Nie,[7] Florent Ginhoux,[3,8,9,10] Yixue Li,[2,11,12,*] Hong Li,[2,*] and Lijian Hui[1,11,13,14,16,*]

[1]State Key Laboratory of Cell Biology, Shanghai Institute of Biochemistry and Cell Biology, Center for Excellence in Molecular Cell Science, Chinese Academy of Sciences, University of Chinese Academy of Sciences, Shanghai 200031, China

[2]CAS Key Laboratory of Computational Biology, Shanghai Institute of Nutrition and Health, University of Chinese Academy of Sciences, Chinese Academy of Sciences, Shanghai 200031, China

[3]Shanghai Institute of Immunology, Department of Immunology and Microbiology, Shanghai Jiao Tong University School of Medicine, Shanghai 200025, China

[4]Beijing Advanced Innovation Center for Genomics (ICG), College of Life Sciences, Department of Obstetrics and Gynecology, Third Hospital, Peking University, Beijing 100871, China

[5]Division of Gastroenterology and Hepatology, Key Laboratory of Gastroenterology and Hepatology, Ministry of Health, State Key Laboratory for Oncogenes and Related Genes, Renji Hospital, School of Medicine, Shanghai Jiao Tong University, Shanghai Institute of Digestive Disease, Shanghai 200001, China

[6]Department of Oral & Cranio-maxillofacial Surgery, Shanghai Ninth People's Hospital, Shanghai Jiao Tong University School of Medicine, Shanghai 200011, China

[7]State Key Laboratory of Cardiovascular Disease, Fuwai Hospital, National Center for Cardiovascular Disease, Chinese Academy of Medical Sciences and Peking Union Medical College, Beijing 100037, China

[8]Singapore Immunology Network, Agency for Science, Technology and Research, Singapore 138648, Singapore

[9]Translational Immunology Institute, Singhealth/Duke-NUS Academic Medical Centre, Singapore 169856, Singapore

[10]Gustave Roussy Cancer Campus, Villejuif 94800, France

[11]Key Laboratory of Systems Health Science of Zhejiang Province, School of Life Science, Hangzhou Institute for Advanced Study, University of Chinese Academy of Sciences, Hangzhou 310024, China

[12]Guangdong Laboratory, Guangzhou 510320, China

[13]Institute for Stem Cell and Regeneration, Chinese Academy of Sciences, Beijing 100101, China

[14]School of Life Science and Technology, ShanghaiTech University, Shanghai 201210, China

[15]These authors contributed equally

[16]Lead contact

*Correspondence: yxli@sibs.ac.cn (Y.L.), lihong01@sibs.ac.cn (H.L.), ljhui@sibcb.ac.cn (L.H.)

https://doi.org/10.1016/j.stem.2023.01.009

SUMMARY

Stem cell-independent reprogramming of differentiated cells has recently been identified as an important paradigm for repairing injured tissues. Following periportal injury, mature hepatocytes re-activate reprogramming/progenitor-related genes (RRGs) and dedifferentiate into liver progenitor-like cells (LPLCs) in both mice and humans, which contribute remarkably to regeneration. However, it remains unknown which and how external factors trigger hepatocyte reprogramming. Here, by employing single-cell transcriptional profiling and lineage-specific deletion tools, we uncovered that periportal-specific LPLC formation was initiated by regionally activated Kupffer cells but not peripheral monocyte-derived macrophages. Unexpectedly, using *in vivo* screening, the proinflammatory factor IL-6 was identified as the niche signal repurposed for RRG induction via STAT3 activation, which drove RRG expression through binding to their pre-accessible enhancers. Notably, RRGs were activated through injury-specific rather than liver embryogenesis-related enhancers. Collectively, these findings depict an injury-specific niche signal and the inflammation-mediated transcription in driving the conversion of hepatocytes into a progenitor phenotype.

INTRODUCTION

The reprogramming of differentiated cells into progenitor-like cells has recently been discovered as an important injury-repair paradigm independent of adult stem cells in a variety of epithelial tissues in mammals,[1] such as the lung,[2] intestine,[3] pancreas,[4] and liver.[5,6] A better understanding of *in vivo* reprogramming would not only provide new insights into tissue repair but also

Please cite this article in press as: Li et al., Kupffer-cell-derived IL-6 is repurposed for hepatocyte dedifferentiation via activating progenitor genes from injury-specific enhancers, Cell Stem Cell (2023), https://doi.org/10.1016/j.stem.2023.01.009

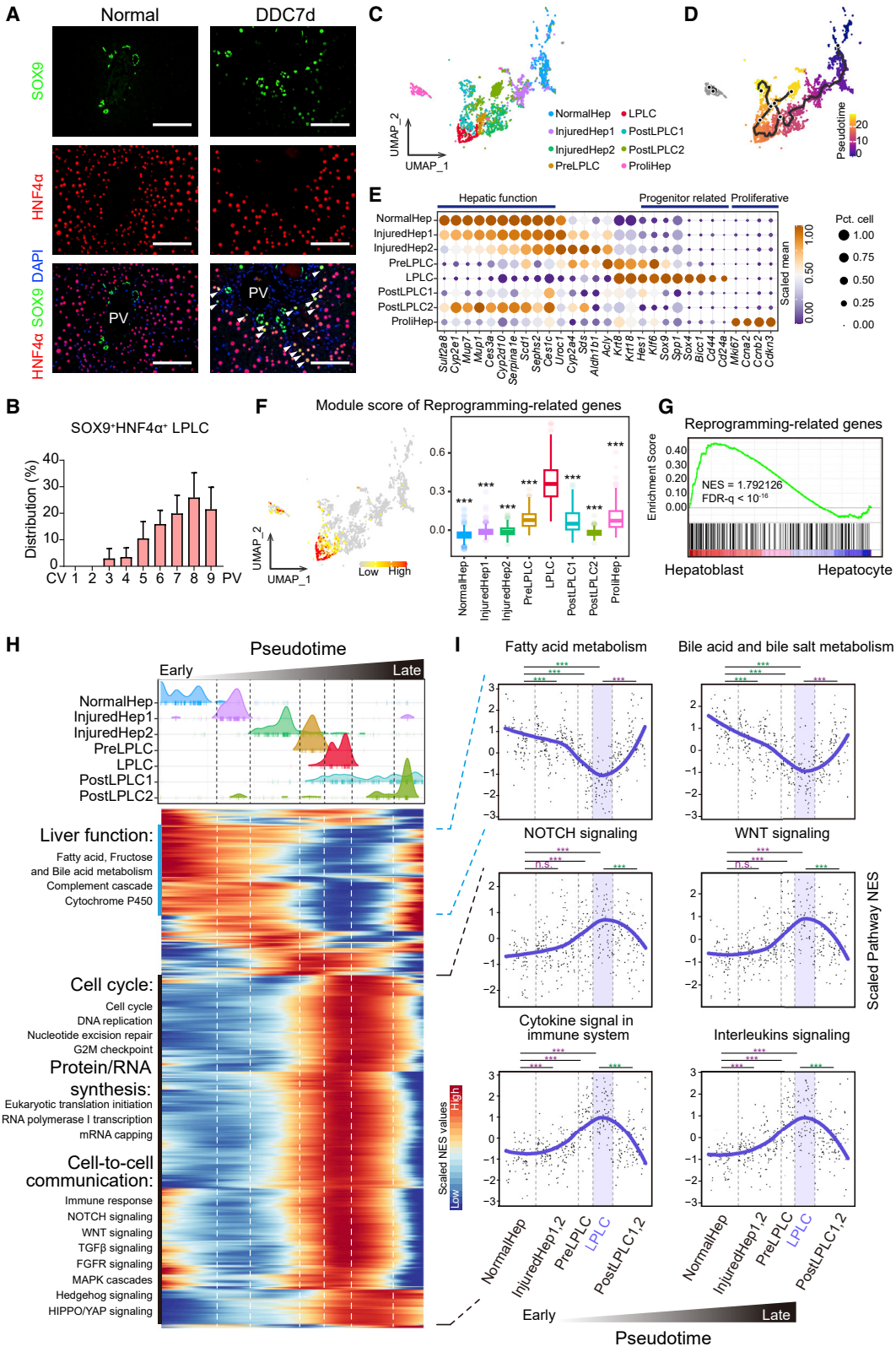

Figure 1. Single-cell analysis of hepatocytes in reprogramming

(A) Co-staining of SOX9 and HNF4α in normal and DDC-injured livers. CV, central vein; PV, portal vein. Scale bars: 100 μm.

(B) The distribution of SOX9⁺HNF4α⁺ LPLCs across the liver lobular (n = 8).

(legend continued on next page)

Please cite this article in press as: Li et al., Kupffer-cell-derived IL-6 is repurposed for hepatocyte dedifferentiation via activating progenitor genes from injury-specific enhancers, Cell Stem Cell (2023), https://doi.org/10.1016/j.stem.2023.01.009

facilitate the development of therapies for diseases related to impaired regeneration. However, by which mechanism the reprogramming of differentiated cells is triggered remains largely uncharacterized.

The liver possesses a remarkable regeneration capacity under injury conditions. Following periportal injury, hepatocytes reactivated progenitor genes and underwent dedifferentiation into liver progenitor-like cells (LPLCs) to repair the injured liver. For example, in 3,5-diethoxycarbonyl-1,4-dihydrocollidin (DDC)-induced periportal injury, LPLCs gave rise to approximately 25% of the newly regenerated hepatocytes and, to some extent, cholangiocytes.[7,8] When the formation of LPLCs was restrained, injured livers showed prolonged hepatocyte proliferation, enhanced biliary injury, and reduced fibrosis resolution.[8] It is noteworthy that LPLCs were also detected in various human liver diseases, suggesting the relevance of these cells in human pathogenesis.[9] However, despite their significance in periportal injury and repair, the molecular mechanisms underlying hepatocyte reprogramming remain largely uncharacterized.

Our previous study has revealed that the chromatin regions of liver progenitor genes remain accessible in mature hepatocytes, thereby endowing hepatocytes with intrinsic "reprogramming competence" for the rapid response to extrinsic injury signals and expression of these genes.[8] Several extrinsic signals have been proposed for LPLC formation, including Notch and Wnt.[9,10] However, these signals exist under both pathological and physiological conditions, leading to the question of whether there are injury-specific signals for LPLC induction. In addition, cell reprogramming often occurs in highly specialized regions of injured tissues.[11] In periportal injury, LPLCs are mainly generated in the region 1–5 layers away from injured bile ducts.[7–9,12,13] Given the anatomically specialized formation of LPLCs, it is reasonable to speculate that there is a region-specific niche signal that drives LPLC formation.

In addition to the unidentified driving signal, it is important to understand how such a signal is transduced to produce a dedifferentiated phenotype from mature hepatocytes. As shown by *in vitro* reprogramming systems, such as induced pluripotent stem cells[14,15] and induced hepatocytes,[14,15] original cells were converted to other cell identities by directly overexpressing a set of lineage-specific transcription factors. However, it is difficult to imagine the direct overexpression of progenitor-specific transcription factors in injury-induced reprogramming *in vivo*. Instead, either signals specific for the reprogramming or the repurposing of known signals are expected. In addition, since the dedifferentiation of mature hepatocytes re-activates genes highly expressed in liver embryogenesis, it is important to determine whether such a signal controls the regulatory mechanism that is shared between development and reprogramming.[16] Nevertheless, if an injury-specific signal triggers hepatocyte reprogramming, should we rather expect a development-independent regulation driving the expression of progenitor genes in injured adult livers?

In this study, by employing single-cell RNA sequencing (scRNA-seq) and lineage-specific mouse lines, we identified that a subpopulation of liver-resident macrophages (Kupffer cells, KCs), locating around injured bile ducts, provided a periportal-specific niche for hepatocyte reprogramming. Surprisingly, using *in vivo* screening, we identified that the proinflammatory factor IL-6, as the key niche signal secreted by regionally activated KCs, but not by monocyte-derived macrophages (MoMFs), was repurposed to induce the expression of reprogramming/progenitor-related genes (RRGs) through STAT3 activation. Importantly, STAT3, which was inactivated in hepatocyte specification during liver embryogenesis, drove reprogramming through directly binding to pre-accessible enhancers of RRGs, demonstrating an injury-specific rather than development-related transcriptional regulation.

RESULTS

Dynamic cellular responses in hepatocyte reprogramming

To delineate hepatocyte reprogramming, we characterized the molecular features and activated pathways in LPLCs during periportal liver injury and inversely inferred extrinsic trigger signals based on the activated pathways. LPLCs, formed specifically around periportal regions, were determined as parenchymal cells both showing a hepatocyte morphology and expressing both the hepatic marker HNF4α, and the progenitor marker SOX9 (Figures 1A and 1B).[7–9] Hepatocytes were collected from livers after 1 week of DDC injury, at which time LPLCs were fully induced (Figure S1A). Normal hepatocytes were used as controls. 10X Chromium scRNA-seq was performed to unbiasedly obtain gene expression profiles during hepatocyte reprogramming (Figures 1C and S1B). After quality control and data filtration, we retained 1,194 cells from normal livers and 3,606 cells from DDC-injured livers for subsequent analyses (STAR Methods).

Twenty-five cell clusters were identified by a graph-based algorithm and visualized using uniform manifold approximation and projection (UMAP; Figure S1C). Cells of clusters 0, 11, 12, 14, 15, 22, 23, and 24 showing high expression of liver function genes, such as *Sult2a8*, *Mup7* and *Mup1*, were designated as normal hepatocytes (NormalHep; Figures S1D and S1E). Notably, NormalHep showed low expression levels of stress response genes[17] activated during tissue dissociation (Figure S1F), suggesting limited hepatocyte damage during isolation. Using the well-established progenitor markers, *Sox9*, *Spp1*, *Sox4*, *Bicc1*, *Cd44*, and *Cd24a*, cluster 7 was annotated

(C and D) UMAP visualization of hepatocytes in normal and DDC-injured livers generated by 10X chromium protocol. Colors indicated cell subpopulations (C) or pseudotime (D).
(E) Dot plot showing the scaled expression levels of feature genes among cell subpopulations.
(F) Module scores of RRGs in each cell were exhibited on UMAP (left) and boxplot (right).
(G) The GSEA analysis of RRGs in hepatoblast versus hepatocyte.
(H) Heatmap showing the scaled activity of pathways in reprogramming.
(I) Scatterplots showing the dynamic changing patterns of representative signaling pathways along reprogramming pseudotime.
n.s., not significant; ***$p < 0.001$. See also Figure S1; Tables S1 and S2.

Please cite this article in press as: Li et al., Kupffer-cell-derived IL-6 is repurposed for hepatocyte dedifferentiation via activating progenitor genes from injury-specific enhancers, Cell Stem Cell (2023), https://doi.org/10.1016/j.stem.2023.01.009

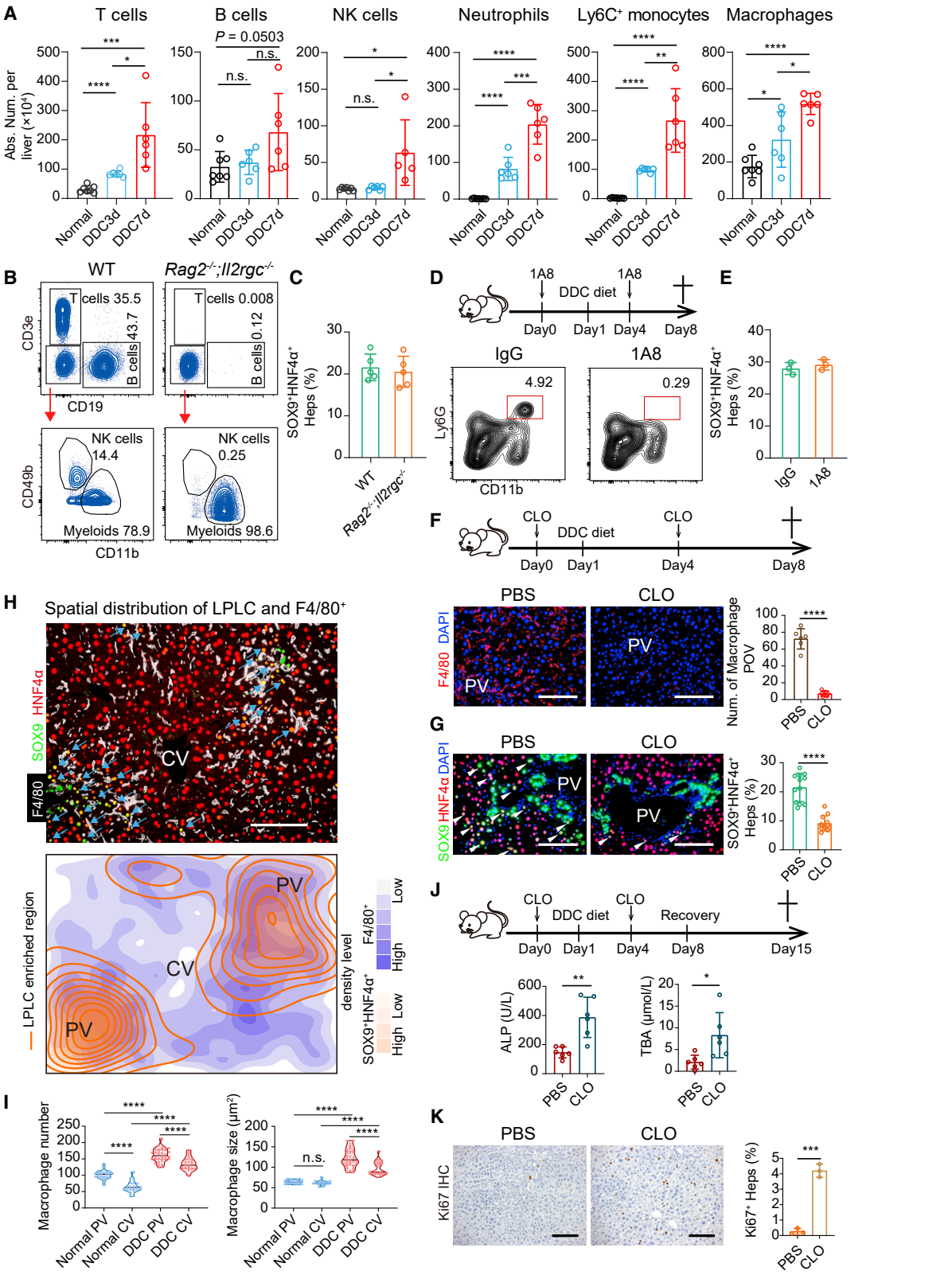

(legend on next page)

Please cite this article in press as: Li et al., Kupffer-cell-derived IL-6 is repurposed for hepatocyte dedifferentiation via activating progenitor genes from injury-specific enhancers, Cell Stem Cell (2023), https://doi.org/10.1016/j.stem.2023.01.009

as LPLCs (Figure S1E). To unravel the cellular transitions during reprogramming, we performed pseudotime ordering of the hepatocytes (Figure 1D; STAR Methods). The reprogramming trajectory showed that normal hepatocytes projected through injured hepatocytes (InjuredHep1 and InjuredHep2), PreLPLCs to LPLCs, which then progressed to the stage showing reduced expression of progenitor markers (PostLPLC1 and PostLPLC2; Figure 1D). Consistently, the enhanced expression of progenitor genes and downregulated liver function genes correlated with the continuous transition between different subpopulations (Figure 1E).

Based on this dataset, we identified 232 RRGs enriched in LPLCs (Table S1; STAR Methods). RRGs significantly distinguished LPLCs from other subpopulations, as LPLCs showed the highest module score of RRGs (Figure 1F). RRGs represented key features of reprogramming, such as genes related to liver progenitors, fetal liver functions, epithelial cell differentiation, cell proliferation and adhesion (Figure S1G; Table S1). Notably, we validated that RRGs were enriched in hepatoblasts by analyzing the expression of E12.5 fetal livers (Figure 1G), confirming that hepatocyte reprogramming re-activated genes expressed during liver embryogenesis.

To infer potential trigger signals for LPLC formation, we deciphered the dynamics of pathway activation during reprogramming by single-sample gene set enrichment analysis (Table S2; STAR Methods). Several reported injury-related pathways were activated, including the Notch, Wnt, TGF-β and Hippo/Yap pathways (Figures 1H and 1I). Importantly, it was notable that immune-related pathways exhibited remarkably dynamic patterns. Upon damage, immune responses were significantly activated in InjuredHeps, which were further enhanced in PreLPLCs and showed the strongest activation in LPLCs (Figures 1I and S1H). Notably, the proinflammatory IL-6 and TNF response pathways were not immediately induced in InjuredHeps but were gradually elevated in PreLPLCs and LPLCs (Figure S1H), displaying patterns closely correlated with LPLC formation. These data indicated that immune-related pathways were activated in a stage-dependent manner during LPLC formation.

To obtain in-depth coverage of the altered genes, LPLCs were isolated from DDC-injured *Sox9-EGFP* mice and were analyzed by Smart-seq2 (Figures S1I–S1K; STAR Methods). A trajectory from normal hepatocytes to LPLCs was identified using this dataset (Figure S1L), and the module score of RRGs also distinguished LPLCs from non-LPLCs (Figure S1M). Importantly, immune-related pathways were again markedly increased, supporting a correlation between immune response and LPLC formation (Figure S1N).

Macrophages drive hepatocyte reprogramming

The strong immune response in LPLCs led us to postulate that immune signals may play a role in reprogramming. We then analyzed the dynamic alterations in immune cell populations by absolute number quantification. In line with the elevated immune response, numbers of innate immune cells, including macrophages, neutrophils, and natural killer (NK) cells, and adaptive immune cells, including T cells and B cells, were increased in injured livers (Figure 2A; STAR Methods).

We characterized which types of immune cells might be involved in hepatocyte reprogramming. *Rag2*$^{-/-}$*;Il2rgc*$^{-/-}$ mice deficient in T cells, B cells, and NK cells were analyzed (Figure 2B). LPLC formation in DDC-injured *Rag2*$^{-/-}$*;Il2rgc*$^{-/-}$ mice, *Rag2*$^{-/-}$ mice, and *Il2rgc*$^{-/-}$ mice was comparable to that in wild-type (WT) mice as indicated by quantification of SOX9^{+}HNF4α^{+} cells (Figures 2C and S2A). To investigate whether neutrophils were involved, the anti-Ly6G antibody 1A8 was utilized to deplete neutrophils (Figure 2D). LPLC formation was not affected by neutrophil depletion (Figure 2E). These data suggested that T cells, B cells, NK cells, and neutrophils are dispensable for hepatocyte reprogramming. When liver macrophages were efficiently depleted by clodronate liposomes (Figure 2F), LPLC formation was reduced by 57.7% (Figure 2G). In another periportal liver injury model induced by 4,4′-diaminodiphenylmethane (DAPM), macrophage depletion also led to a substantial decrease in LPLC formation (Figure S2B), suggesting that macrophages are required for LPLC formation in multiple injuries.

We next performed scRNA-seq of hepatocytes from macrophage-depleted DDC-injured livers (Figure S2C). Integration analysis mapped these cells into subpopulations determined in Figure 1C (STAR Methods). When visualized on UMAP, a subpopulation of hepatocytes from macrophage-depleted livers (cluster 4) was identified sharing the same area where LPLCs were located (Figure S2C). However, compared with LPLCs, the expression of RRGs and immune-related pathways was not fully induced in cluster 4 (Figures S2D and S2E). When individual subpopulations were analyzed, the expression of pathways upregulated during reprogramming was reduced in hepatocytes from macrophage-depleted livers (Figure S2E). In

Figure 2. Macrophages control hepatocyte reprogramming

(A) Flow cytometry showed the absolute number of T cells (CD45^{+}CD3e^{+}), B cells (CD45^{+}CD19^{+}), NK cells (CD45^{+}NK1.1^{+}), neutrophils (CD45^{+}CD11b^{+}Ly6G^{+}), Ly6C^{+} monocytes (CD45^{+}Ly6G^{-}CD11b^{+}F4/80^{-}Ly6C^{+}), and macrophages (CD45^{+}CD11b^{low}Ly6G^{-}F4/80^{+}) in normal (n = 7), 3-day DDC-injured (n = 6) and 7-day DDC-injured (n = 6) livers.

(B and C) The depletion efficiency of T cells, B cells, and NK cells was analyzed in peripheral blood (B). The ratios of SOX9^{+}HNF4α^{+} cells in DDC-injured livers were quantified (C; n = 5).

(D and E) Neutrophils depletion and DDC injury. The depletion efficiency of neutrophils was analyzed by flow cytometry (D). The ratios of SOX9^{+}HNF4α^{+} cells were quantified (E; n = 3).

(F and G) Macrophage depletion and DDC injury. Immunofluorescent staining of F4/80 and the number of F4/80^{+} cells per field of view (POV) were shown (F; n = 6). Co-staining of SOX9 and HNF4α and the ratios of SOX9^{+}HNF4α^{+} cells were shown (G; n = 12). CLO, clodronate liposomes; PBS, PBS liposomes.

(H) Co-staining of SOX9, HNF4α, and F4/80 in DDC-injured livers. The corresponding density plot image was shown.

(I) The mean number (left) and size (right) of macrophages around PV or CV were quantified (n = 5). Each circle denoted the number in a field of view.

(J and K) Macrophage depletion and post-injury recovery. Serum levels of ALP and TBA were measured (J; n = 6). Immunohistochemistry staining of Ki67 and the ratios of Ki67^{+} hepatocytes were shown (K; n = 3).

Scale bars: 100 μm. Data were presented as mean ± SD; n.s., not significant; *p < 0.05, **p < 0.01, ***p < 0.001, ****p < 0.0001, t test. See also Figure S2.

Please cite this article in press as: Li et al., Kupffer-cell-derived IL-6 is repurposed for hepatocyte dedifferentiation via activating progenitor genes from injury-specific enhancers, Cell Stem Cell (2023), https://doi.org/10.1016/j.stem.2023.01.009

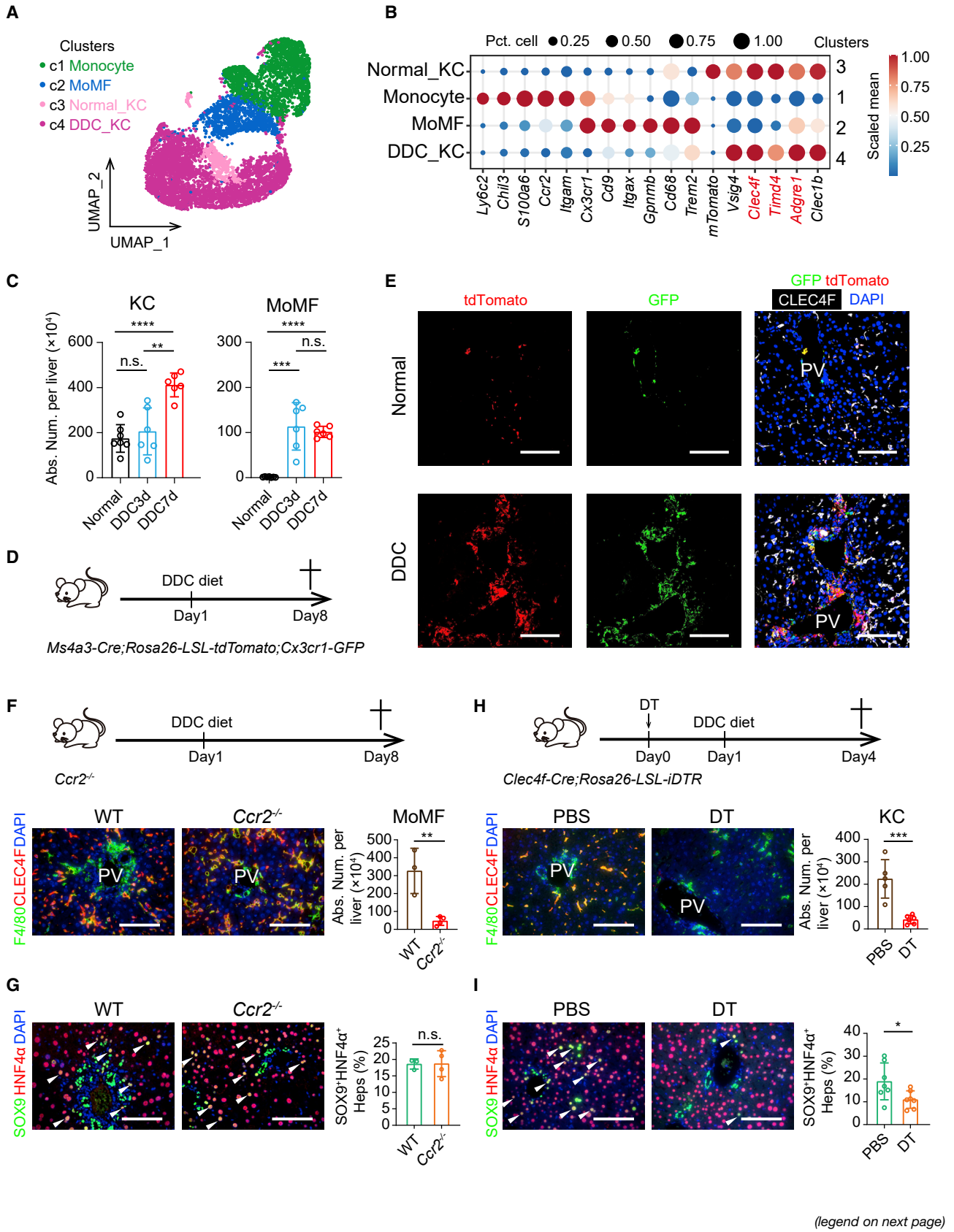

(legend on next page)

Please cite this article in press as: Li et al., Kupffer-cell-derived IL-6 is repurposed for hepatocyte dedifferentiation via activating progenitor genes from injury-specific enhancers, Cell Stem Cell (2023), https://doi.org/10.1016/j.stem.2023.01.009

contrast, liver function pathways remained relatively high in cluster 4 (Figure S2E). These data support that LPLC formation is impeded by macrophage depletion.

We then analyzed the spatial correlation between macrophages and LPLCs. F4/80 staining showed that macrophages were significantly enriched in the periportal regions (Figures 2H and 2I), where LPLCs were formed (Figure 1B). Moreover, periportal macrophages exhibited a significantly larger cellular size compared with those around the central veins (Figure 2I), suggesting that these macrophages might constitute a regional reprogramming niche.

Because hepatocyte reprogramming is required for liver repair,[7,8] we speculated that reduced formation of LPLCs after macrophage depletion would lead to impaired post-injury repair. Compared with control mice, serum levels of alkaline phosphatase (ALP), total bile acid (TBA), alanine aminotransferase (ALT), and aspartate aminotransferase (AST) stayed high in macrophage-depleted mice after DDC withdrawal at multiple time points (Figures 2J and S2F–S2J). No differences in serum bilirubin levels, glucose levels, and activated partial thromboplastin time were detected during the recovery (Figures S2K–S2M). The ratio of Ki67$^+$ hepatocytes was decreased at 1 week after DDC injury but remained to be continuously detectable at higher levels in macrophage-depleted mice (Figures 2K and S2N). The higher ratio of Ki67$^+$ hepatocytes after DDC withdrawal appeared to be correlated with the decreased reprogramming and unresolved injury in these mice. These data supported that macrophage depletion, which resulted in dysregulated hepatocyte reprogramming, led to impaired liver repair after periportal injury.

Resident KCs are the subtype of macrophages required for LPLC formation

Two subtypes of macrophages have been identified in injured livers: KCs and MoMFs.[18] These macrophages function differently in tissue injury and regeneration.[18,19] To investigate the composition of liver macrophages in DDC-induced injury, we performed scRNA-seq of 10,210 macrophages and related cells from normal and DDC-injured livers (Figures 3A and S3A; STAR Methods). In DDC-injured livers, three clusters were identified. Cluster 4, expressing KC markers *Clec4f*, *Timd4*, and *Vsig4*,[20] was denoted as DDC_KC (Figure 3B). Cluster 2, negative for KC markers and positive for macrophage markers *Adgre1*, *Trem2*, *Cd68*, *Gpnmb*, and *Cx3cr1*, was designated as MoMF[21] (Figure 3B). Cluster 1, positive for *Ccr2*, *Itgam*, *S100a6*, *Cx3cr1*, and *Ly6c2* and negative for macrophage markers, was designated as monocytes,[20] the precursors of MoMFs (Figure 3B). In normal livers, only one cluster showing high expression levels of KC markers was identified and designated as Normal_KC (Cluster 3; Figure 3B).

The number of KCs remained unchanged at day 3 and increased 2.4-fold at 1 week (Figure 3C), likely due to the augmented proliferation of KCs in injured livers (Figures S3B–S3D). MoMFs were almost undetectable in normal livers, whereas around 1 × 10^6 MoMFs were recruited per injured liver as early as three days after injury (Figure 3C). We further determined whether the spatial localization of KCs and MoMFs correlated with LPLCs. CLEC4F staining revealed that KCs were localized across the lobule in injured livers (Figures S3E and S3F). When monocytes and MoMFs were labeled as tdTomato$^+$GFP$^+$ using *Ms4a3-Cre;Rosa26-LSL-tdTomato;Cx3cr1-GFP* mice, these cells were recruited to the portal veins after DDC treatment (Figures 3D and 3E). In addition, co-staining with F4/80 and CLEC4F confirmed that MoMFs (F4/80$^+$CLEC4F$^-$) were located close to the portal veins (Figures S3G and S3H). These data imply that both KCs and MoMFs are possible niche cells driving hepatocyte reprogramming.

To unambiguously distinguish the roles of these two cell subtypes, we applied lineage-specific mouse lines to either block the recruitment of monocytes or deplete KCs. As liver infiltration of monocytes depends on CCR2 signaling,[22] we used *Ccr2*$^{-/-}$ mice to block the recruitment of MoMFs into injured livers. *Ccr2*$^{-/-}$ mice displayed a reduced number of MoMFs after DDC injury (Figure 3F), while the KC population was not altered (Figure S3I). Interestingly, LPLC formation remained unchanged in DDC-injured *Ccr2*$^{-/-}$ livers (Figure 3G), largely excluding the role of MoMFs in LPLC induction. Next, KCs were efficiently depleted in *Clec4f-Cre;Rosa26-LSL-iDTR* mice by diphtheria toxin treatment (Figure 3H). Notably, DDC-induced LPLC formation was significantly reduced after KC depletion (Figure 3I), suggesting a key role of KCs in hepatocyte reprogramming.

IL-6 derived from activated periportal KCs triggers reprogramming

We then analyzed by which factor KCs induced hepatocyte dedifferentiation. Based on the above results, this factor should be paracrinely produced from KCs, but not from MoMFs or other

Figure 3. Resident Kupffer cells are the subtype of macrophages required for LPLC formation

(A) UMAP visualization of macrophages/monocytes in normal and DDC-injured livers from 10X chromium sequencing.

(B) Dot plot showing the scaled gene expression levels of lineage-specific marker genes in different subpopulations. *mTomato*$^+$, cells from normal livers; *mTomato*$^-$, cells from injured livers.

(C) The absolute number of KCs (CD45$^+$Lin$^-$CD11b^{low}F4/80$^+$Tim4$^+$, left) and MoMFs (CD45$^+$Lin$^-$CD11b^{low}F4/80$^+$Tim4$^-$, right) in normal (n = 7) and DDC-injured (n = 6) livers were shown.

(D and E) MoMFs/monocytes were traced as tdTomato$^+$GFP$^+$ in *Ms4a3-Cre;Rosa26-LSL-tdTomato;Cx3cr1-GFP* mice (D). Immunofluorescent staining of CLEC4F was shown (E). n = 3.

(F and G) DDC injury in WT and *Ccr2*$^{-/-}$ mice. Co-staining of F4/80 and CLEC4F and the quantification of absolute number of MoMFs (CD45$^+$Lin$^-$CD11b^{low}F4/80$^+$Tim4$^-$) per mice by flow cytometry were shown (F; right). Co-staining of SOX9 and HNF4α and the ratios of SOX9$^+$HNF4α$^+$ cells were shown (G). WT, n = 3; *Ccr2*$^{-/-}$, n = 4.

(H and I) DDC injury after PBS or diphtheria toxin (DT) treatment in *Clec4f-Cre;Rosa26-LSL-iDTR* mice. Co-staining of F4/80 and CLEC4F and the quantification of absolute number of KCs per mice by flow cytometry were shown (H; PBS, n = 5; DT, n = 6). Co-staining of SOX9 and HNF4α and the ratios of SOX9$^+$HNF4α$^+$ cells were shown (I; n = 7).

Scale bars: 100 μm. Data were presented as mean ± SD; n.s., not significant; *p < 0.05, **p < 0.01, ***p < 0.001, ****p < 0.0001, t test. See also Figure S3.

Please cite this article in press as: Li et al., Kupffer-cell-derived IL-6 is repurposed for hepatocyte dedifferentiation via activating progenitor genes from injury-specific enhancers, Cell Stem Cell (2023), https://doi.org/10.1016/j.stem.2023.01.009

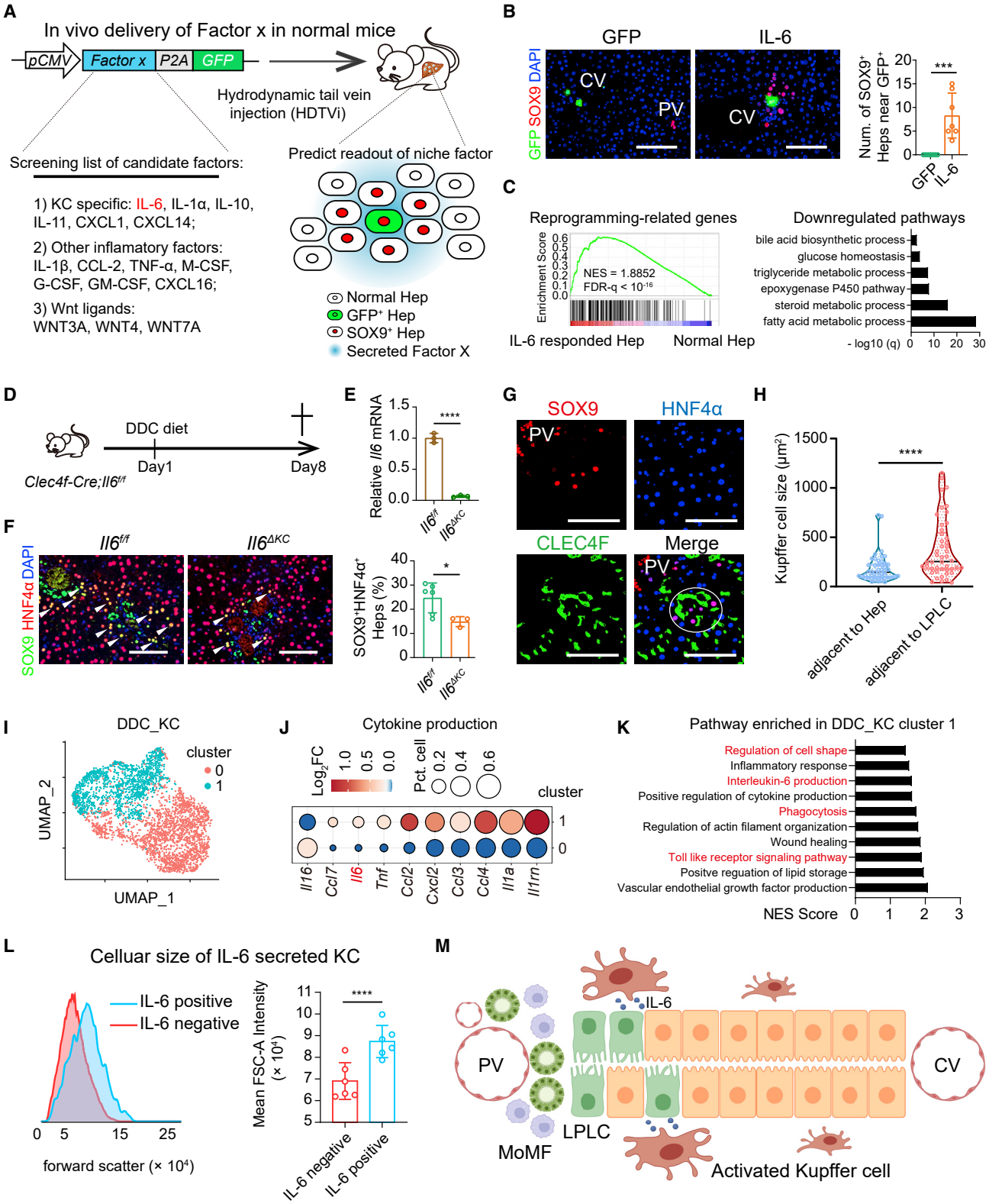

Figure 4. IL-6 derived from regionally activated Kupffer cells triggers hepatocyte reprogramming

(A) Schematic view of *in vivo* delivery of factors in normal mice.

(B) Co-staining of SOX9 and GFP in livers of HDTVi of GFP (CMV-*GFP*) or IL-6 (CMV-*Il6-GFP*). The number of SOX9$^+$ hepatocytes near GFP$^+$ cells was quantified (n = 7).

(legend continued on next page)

Please cite this article in press as: Li et al., Kupffer-cell-derived IL-6 is repurposed for hepatocyte dedifferentiation via activating progenitor genes from injury-specific enhancers, Cell Stem Cell (2023), https://doi.org/10.1016/j.stem.2023.01.009

immune cells. scRNA-seq of macrophages from DDC-injured livers suggested a set of KC-specific secretion factors, including IL-1a, IL-1b, and IL-6 (Figure S3J). Additionally, transcriptome analyses of macrophages, monocytes, T cells, and neutrophils from injured livers showed another set of factors expressed in macrophages but not in T cells or neutrophils (Figure S3K). In total, 13 inflammatory factors were selected as candidate factors, and 3 Wnt ligands commonly expressed in the liver were additionally included (Figure 4A).

To identify the factors that trigger reprogramming, we expressed each factor individually in normal livers (Figure 4A). Genes encoding candidate factors were cloned into a vector carrying the GFP reporter and then delivered to the liver by hydrodynamic tail-vein injection (HDTVi; STAR Methods). The GFP reporter without candidate factor was used as the control. Co-staining of GFP and HNF4α in HDTVi livers showed that 98.5% of GFP$^+$ cells were HNF4α^+ hepatocytes (Figure S4A). In this system, hepatocytes were used as a proxy to secrete the factor without injury context, so that we could determine the driving effect of the factor on hepatocyte reprogramming. To specify the niche effect of the factor, cells were sparsely transfected into the liver using a low dose of vector. We speculated that if the factor could trigger reprogramming, SOX9$^+$ hepatocytes should be detected around GFP-positive cells secreting this factor.

Among the 16 factors, IL-6 was the only factor that robustly induced SOX9$^+$HNF4α^+ hepatocytes (Figure 4B). Notably, all SOX9$^+$HNF4α^+ hepatocytes formed neighboring IL-6-secreting cells, showing a paracrine effect. Other inflammatory factors and Wnt ligands, when expressed alone, did not induce the formation of SOX9$^+$HNF4α^+ cells (Figure S4B). It was remarkable that these cells highly expressed *Il6* (Figure S4C) and RRGs (Figure 4C), including the progenitor marker genes—*Sox9*, *Spp1*, *Bicc1*, *Cd44*, and *Cd24a*—and displayed dramatically downregulated liver function pathways (Figure 4C), confirming that IL-6 induces hepatocyte reprogramming.

To determine the specificity of KC-derived IL-6, we validated that the expression of *Il6* was increased at the beginning of DDC injury by qRT-PCR (Figure S4D) and that IL-6 was produced from KCs, but not other types of cells, by measuring IL-6 protein levels in all non-parenchymal cells from injured livers (Figures S4E and S4F). IL-6 was specifically deleted in KCs using *Clec4f-Cre;Il6$^{f/f}$* (*Il6$^{\Delta kc}$*) mice (Figures 4D and 4E). *Il6* deletion did not affect KC numbers and the expression of KC activated genes (Figures S4G and S4H). The formation of DDC-induced LPLCs was significantly reduced in *Il6$^{\Delta kc}$* livers (Figure 4F). The reduction in LPLC formation was at the level comparable to that in mice with macrophage depletion (Figure 2G) or KC depletion (Figure 3I). These data suggested that KC-derived IL-6 is a major niche factor in LPLC induction.

Given that KCs were distributed across the lobule in the injured livers (Figure S3F), whereas LPLCs were formed specifically in the periportal regions (Figure 1B), we speculated that KCs were differentially activated to secrete IL-6. Notably, co-staining of KCs and LPLCs revealed that KCs adjacent to LPLCs exhibited a significantly enlarged cellular size (Figures 4G and 4H), indicating that these KCs might be activated during injury. Moreover, two subpopulations within the DDC-treated KCs were unbiasedly identified using scRNA-seq data (Figure 4I). Cluster 1 of DDC_KCs, expressing feature genes such as *Cd38*, *Mmp12*, *Egr1*, *Nr4a1*, and *Cd80* (Figure S4I), showed upregulated levels of inflammatory cytokine genes, including *Il6*, *Tnf*, and *Il1a* (Figure 4J). Pathway analysis also confirmed the enrichment of phagocytosis, IL-6 production, and the TLR pathway in this subpopulation (Figure 4K; Table S3). Interestingly, IL-6-positive KCs exhibited a larger cellular size than IL-6-negative KCs (Figure 4L), which was consistent with the enlarged size of KCs adjacent to LPLCs *in situ* (Figure 4G). During liver injury, KCs could be activated by proinflammatory factors and damage-associated molecular patterns (DAMPs) released from injured hepatocytes and cholangiocytes.[19] We additionally analyzed whether DDC directly activated KCs by treating freshly isolated KCs with DDC *in vitro*. Interestingly, *Il6* and other feature genes of activated KCs were induced (Figures S4J and S4K), while the number of KCs appeared unchanged (Figure S4L). Together, these data suggested that following injury an activated and enlarged subset of KCs highly produce IL-6 and induce periportal LPLC formation (Figure 4M).

IL-6 directly affects hepatocyte dedifferentiation

Proper transduction of the IL-6 signal requires IL-6 receptor IL-6RA and co-receptor gp130.[23] Both *Il6ra* and *gp130* were expressed in normal hepatocytes and LPLCs as determined by scRNA-seq analyses (Figure S5A). To confirm that IL-6 interacts with hepatocytes directly (Figure 5A), we specifically deleted IL-6 receptor (IL-6RA) in hepatocytes using *Alb-Cre;Il6ra$^{f/f}$* (*Il6ra$^{\Delta li}$*) mice. *Il6ra* was efficiently deleted in *Il6ra$^{\Delta li}$* livers (Figure S5B) without affecting mature hepatic functions (Figure S5B) or KC population (Figure S5C). In line with the findings in *Il6$^{\Delta kc}$* mice, hepatocyte-specific deletion of IL-6RA significantly decreased the formation of LPLCs (Figure 5B). Moreover, adeno-associated viruses (AAVs) 8-carried Cre recombinase (AAV-Cre; STAR Methods) were delivered into *gp130$^{f/f}$* mice, which deleted

(C) GSEA analysis (left) showed the enrichment of RRGs in SOX9$^+$ hepatocytes from IL-6 HDTVi livers (IL-6-responded Hep) versus GFP HDTVi controls (Normal Hep). Downregulated pathways in IL-6-responded Hep were shown (right).
(D–F) Schematic view of DDC injury in *Il6$^{f/f}$* and *Il6$^{\Delta kc}$* mice (D). The mRNA level of *Il6* in KCs was determined by qRT-PCR (E; n = 3). Co-staining of SOX9 and HNF4α and the ratios of SOX9$^+$HNF4α^+ cells were shown (F; *Il6$^{f/f}$*, n = 6; *Il6$^{\Delta kc}$*, n = 3).
(G) Co-staining of SOX9, HNF4α, and CLEC4F in DDC-injured mice.
(H) The size of KCs adjacent to SOX9$^-$HNF4a$^+$ hepatocytes and adjacent to SOX9$^+$HNF4a$^+$ LPLCs in DDC-injured livers was quantified (n = 3). Each circle denoted a cell.
(I) UMAP visualization of DDC_KCs (Figure 3A).
(J) Dot plot showing the scaled gene expression levels of cytokine genes in different subpopulations from DDC_KCs.
(K) Pathways enriched in DDC_KC_c1 versus DDC_KC_c0.
(L) Flow cytometry showed the cellular size of IL-6$^+$ KCs and IL-6$^-$ KCs. Mean FSC-A intensity was quantified (n = 6).
(M) Schematic view showed regionally activated KCs produced IL-6 to regulate LPLC formation following injury.
Scale bars: 100 μm. Data were presented as mean ± SD; *p < 0.05, ***p < 0.001, ****p < 0.0001, t test. See also Figures S3 and S4; Table S3.

Please cite this article in press as: Li et al., Kupffer-cell-derived IL-6 is repurposed for hepatocyte dedifferentiation via activating progenitor genes from injury-specific enhancers, Cell Stem Cell (2023), https://doi.org/10.1016/j.stem.2023.01.009

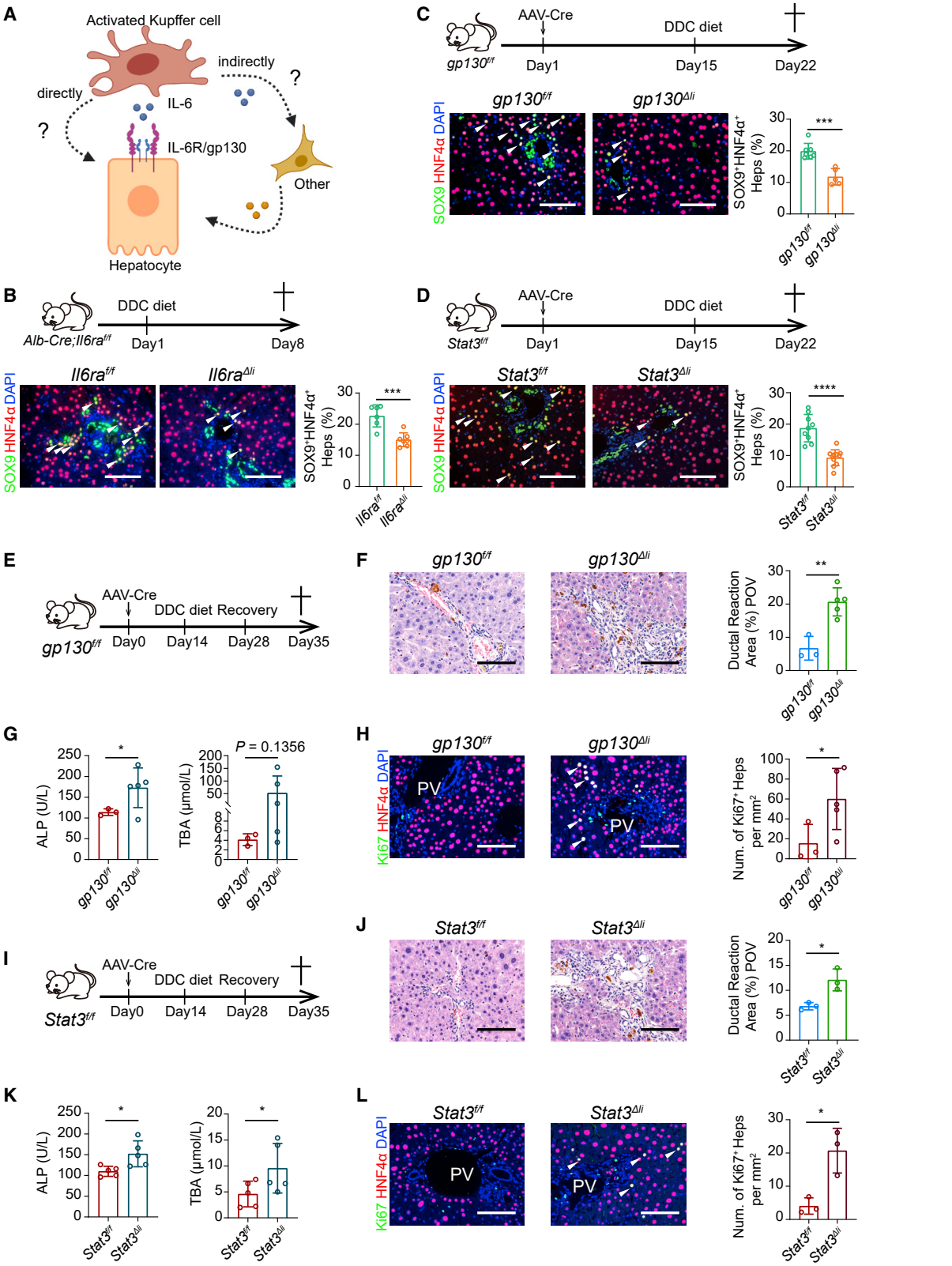

Figure 5. IL-6/STAT3 signaling is repurposed for hepatocyte dedifferentiation and liver repair

(A) Schematic diagram showed the direct and indirect interaction between KCs and hepatocytes.

(B) DDC injury in *Il6ra*$^{f/f}$ and *Il6ra*$^{\Delta li}$ mice. Co-staining of SOX9 and HNF4α and the ratios of SOX9^{+}HNF4α^{+} cells were shown (*Il6ra*$^{f/f}$, n = 6; *Il6ra*$^{\Delta li}$, n = 7).

(legend continued on next page)

gp130 in hepatocytes ($gp130^{\Delta li}$) efficiently and specifically (Figure S5D). Reduced LPLC formation was detected in $gp130^{\Delta li}$ mice after liver injury (Figure 5C). LPLC formation induced by ectopic expression of IL-6 was completely abolished in $Il6ra^{\Delta li}$ and $gp130^{\Delta li}$ mice (Figure S5E). Together, these data demonstrated that KC-derived IL-6 is a key reprogramming niche factor directly inducing hepatocyte reprogramming.

IL-6/STAT3 signaling is repurposed for hepatocyte reprogramming

Binding of IL-6 to IL-6RA and gp130 leads to activation of JAK/STAT3 and, to a lesser extent, YAP.[23] Intriguingly, YAP deletion in hepatocytes did not affect IL-6-induced LPLC formation (Figure S5F). By contrast, immunofluorescent staining of phosphorylated STAT3 (pSTAT3), mainly detectable around the periportal area, confirmed the activation of STAT3 in LPLCs (Figures S5G and S5H). STAT3 activation was strikingly blunted by either depletion of macrophages (Figure S5I) or inhibition of IL-6 signaling (Figure S5J).

To determine whether STAT3 links IL-6 signaling to hepatocyte reprogramming, STAT3 was specifically deleted in hepatocytes by delivering AAV-Cre into $Stat3^{f/f}$ mice ($Stat3^{\Delta li}$). Notably, in $Stat3^{\Delta li}$ mice the number of LPLCs was dramatically reduced following DDC injury (Figure 5D) and completely abolished by IL-6 HDTVi (Figure S5K). In agreement with the reduced hepatocyte reprogramming, transcriptome analysis validated that the induction of RRGs was attenuated in $Stat3^{\Delta li}$ livers from either DDC injury (Figure S5L) or IL-6 HDTVi (Figure S5M). Collectively, these data demonstrated that IL-6/STAT3 proinflammatory signaling is repurposed for hepatocyte reprogramming.

We further investigated whether liver repair would be impaired by the inactivation of STAT3 signaling. To this end, we analyzed liver recovery from DDC injury in $gp130^{\Delta li}$ (Figure 5E) and $Stat3^{\Delta li}$ (Figure 5I) mice. Ductal reaction and fibrosis were still obvious in $gp130^{\Delta li}$ mice (Figure 5F) and $Stat3^{\Delta li}$ mice (Figure 5J) 1 week after recovery. Moreover, liver injury was not fully resolved, as shown by the high serum levels of ALP and TBA and proliferating hepatocytes in $gp130^{\Delta li}$ (Figures 5G and 5H) and $Stat3^{\Delta li}$ mice (Figures 5K and 5L). These results demonstrated the crucial role of IL-6/STAT3 signaling in liver repair after periportal injury.

STAT3 binds to pre-accessible RRG enhancers and reactivates RRG transcription

As IL-6/STAT3 signaling is mainly involved in the proinflammatory response,[23] it was unexpected that it controlled cell identity conversion in liver injury. To define the role of the transcription factor STAT3 in reprogramming, we focused on its regulation on RRGs. LPLCs were induced by HDTVi-mediated IL-6 expression, and chromatin immunoprecipitation sequencing (ChIP-seq) of pSTAT3 was performed specifically in these cells (STAR Methods). We identified 27,685 STAT3-binding sites (corresponding to 11,196 genes) in the genome of LPLCs. Markedly, 186 of 232 RRGs showed STAT3 binding, suggesting a significant increase in STAT3-binding preference for RRGs (Figure 6A; $p = 2.42 \times 10^{-17}$, chi-squared test). Moreover, compared with other STAT3-binding sites, RRGs showed a higher STAT3-binding strength (Figure 6B). Two example loci of RRGs, the upstream regions of *Sox9* and *Spp1*, represented STAT3 binding (Figure 6C).

We previously found that genes expressed in liver progenitors remained accessible in mature hepatocytes via Arid1a regulation, endowing hepatocytes with the competence to respond rapidly to reprogramming signals.[8] We investigated whether IL-6/STAT3-signaling-mediated reprogramming requires Arid1a-controlled chromatin accessibility. Markedly, STAT3-binding sites in RRGs overlapped with Arid1a-opened chromatin sites (Figures 6D and 6E). Moreover, in line with reduced chromatin accessibility in livers lacking *Arid1a*, LPLC formation induced by IL-6 HDTVi was decreased after *Arid1a* deletion (Figure 6F), suggesting that Arid1a-controlled chromatin accessibility is required for IL-6/STAT3-signaling-mediated reprogramming.

Next, we determined whether the binding of STAT3 led to chromatin activation of RRGs by measuring histone 3 acetylation at lysine 27 (H3K27ac), a marker of activated enhancers. STAT3-binding sites in RRGs showed remarkably increased H3K27ac levels in LPLCs (Figures S6A and S6B), suggesting the activation of these sites. To reveal whether the binding of STAT3 imposed transcriptional activation, we analyzed the STAT3-binding sequences of two progenitor marker genes with increased H3K27ac modification (Figure 6G). The upstream regions of the *Sox9* gene (*Sox9-site*) and *Spp1* gene (*Spp1-site*; see Figure 6C) were cloned into the front of an mCherry reporter, which were then transfected into mouse livers (STAR Methods). Upon IL-6 HDTVi, mCherry expression was strongly induced from both *Sox9-site* and *Spp1-site* sequences. Moreover, *Sox9-site*- and *Spp1-site*-driven expression of mCherry was abolished in $Stat3^{\Delta li}$ livers (Figures 6H and S6C), demonstrating that transcription from these enhancers was STAT3 dependent.

STAT3-dependent RRG transcription specifically in liver injury but not in embryogenesis

Genes controlling embryonic development are often reused for adult tissue repair,[16,24] and recent studies have proposed that the transcription of these genes during repair might be regulated

(C) DDC injury in $gp130^{f/f}$ mice treated with AAV-GFP/Cre. Co-staining of SOX9 and HNF4α and the ratios of $SOX9^+HNF4\alpha^+$ cells were shown ($gp130^{f/f}$, n = 7; $gp130^{\Delta li}$, n = 5).

(D) DDC injury in $Stat3^{f/f}$ mice treated with AAV-GFP/Cre. Co-staining of SOX9 and HNF4α and the ratios of $SOX9^+HNF4\alpha^+$ cells were shown ($Stat3^{f/f}$, n = 9; $Stat3^{\Delta li}$, n = 11).

(E–H) Schematic view showed DDC injury and recovery in $gp130^{f/f}$ mice treated with AAV-GFP/Cre (E). H&E staining and ductal reaction area per periportal field of view were shown (F). Serum levels of ALP and TBA were measured (G). Co-staining of Ki67 and HNF4α and the number of $Ki67^+$ hepatocytes were shown (H). $gp130^{f/f}$, n = 3; $gp130^{\Delta li}$, n = 5.

(I–L) Schematic view showed DDC injury and recovery in $Stat3^{f/f}$ mice treated with AAV-GFP/Cre (I). H&E staining and ductal reaction area per periportal field of view were shown (J; n = 3). Serum levels of ALP and TBA were measured (K; n = 5). Co-staining of Ki67 and HNF4α and the number of $Ki67^+$ hepatocytes were shown (L; n = 3).

Scale bars: 100 μm. Data were presented as mean ± SD; *p < 0.05, **p < 0.01, ***p < 0.001, ****p < 0.0001, t test. See also Figure S5.

Please cite this article in press as: Li et al., Kupffer-cell-derived IL-6 is repurposed for hepatocyte dedifferentiation via activating progenitor genes from injury-specific enhancers, Cell Stem Cell (2023), https://doi.org/10.1016/j.stem.2023.01.009

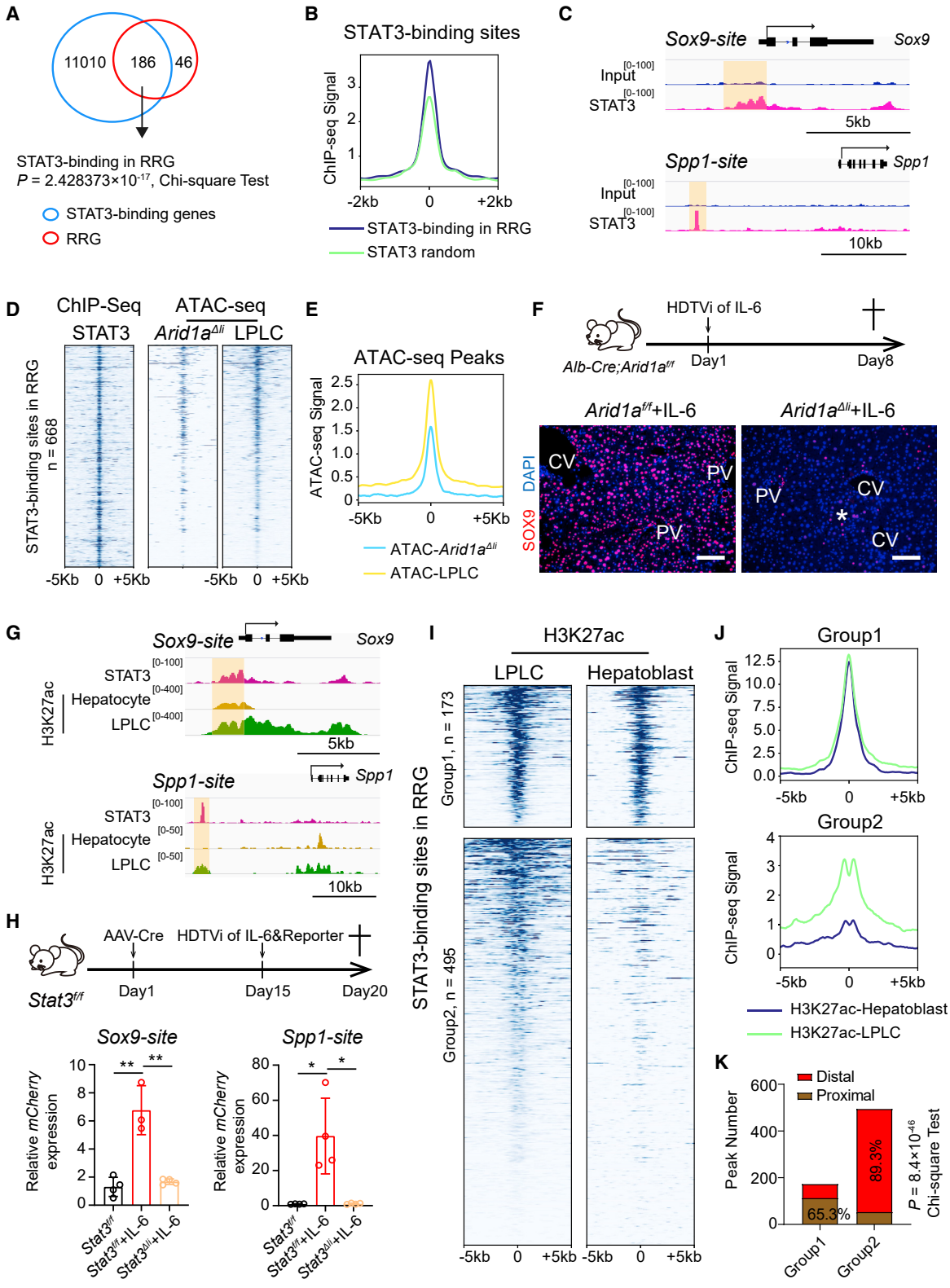

Figure 6. STAT3 re-activates RRG transcription specifically during liver injury

(A) Overlap of STAT3-binding genes by ChIP-seq with RRGs was shown. These genes were referred as STAT3-binding RRGs.

(B) Average STAT3 ChIP-seq signals in RRGs and in 1,000 randomly selected STAT3-binding sites.

(legend continued on next page)

Please cite this article in press as: Li et al., Kupffer-cell-derived IL-6 is repurposed for hepatocyte dedifferentiation via activating progenitor genes from injury-specific enhancers, Cell Stem Cell (2023), https://doi.org/10.1016/j.stem.2023.01.009

by repair-responsive DNA elements.[25–30] Because RRGs were also highly expressed in hepatoblasts during liver embryogenesis (Figure 1G), we investigated whether STAT3-mediated RRG regulation was a development-related or, instead, an injury-specific mechanism. Markedly, in mouse fetal livers, STAT3 was not activated (Figure S6D) and canonical STAT3 target genes[31,32] were not induced (Figure S6E). Furthermore, it was reported that STAT3 was dispensable for liver development.[33] These data indicated that STAT3 is not involved in RRG expression during fetal liver development.

Transcription-factor-mediated gene expression correlates with activated chromatin. As STAT3-mediated RRG transcription is specific in liver repair, we postulated that chromatin activation of RRGs might be regulated differently in LPLCs and hepatoblasts. H3K27ac modifications of RRGs were compared between DDC-induced LPLCs and fetal hepatoblasts. STAT3-binding sites in RRGs showed markedly different patterns of H3K27ac profiles between LPLCs and hepatoblasts (Figure 6I), supporting that chromatin activation of RRGs is regulated differently in regeneration versus development. These chromatin sites were further separated into two groups (Figures 6I and 6J). The first group (173 of 668 STAT3-binding RRG sites) showed similar H3K27ac levels between LPLCs and hepatoblasts (Figure 6J) and was mainly located at proximal regions (Figure 6K). The other group (495 of 668 STAT3-binding RRG sites) showed significantly increased H3K27ac specifically in LPLCs but not in hepatoblasts (Figure 6J). Importantly, most of these sites (89.3%, $p < 8.4 \times 10^{-46}$, chi-squared test) were located at the distal regions of the RRGs (Figure 6K). Since H3K27ac modification reliably marks active enhancers located in the distal regions of a given gene,[34] these data suggested that the binding of STAT3 to RRG enhancers in LPLCs is different from that in hepatoblasts, thereby proposing a transcriptional regulation specific for periportal liver injury and repair.

DISCUSSION

In vivo dedifferentiation and transdifferentiation promise a stem cell-independent paradigm for tissue repair. Many studies have supported the existence of *in vivo* reprogramming in mammalian epithelial tissues. Importantly, mature hepatocytes were found reprogrammed into LPLCs to contribute to liver repair after periportal injury.[7,9,13] We demonstrated here that regionally activated KCs directly induce periportal LPLC formation via IL-6 and that proinflammatory IL-6/STAT3 signaling is repurposed for the expression of RRGs through an injury-specific transcriptional program. IL-6/STAT3 signaling is sufficient to induce a large group of liver progenitor genes, which is an entirely different proinflammatory role for IL-6. These findings provide a paradigm to understand reprogramming in other injured tissues. While sterile inflammation is common in injuries and is often involved in tissue regeneration,[35] our results suggest a concept that proinflammatory signaling may directly induce the transcription of progenitor-related genes for injury-induced cell dedifferentiation in mammals. Given that inflammatory factors are master regulators in the dedifferentiation of mature cells to blastema during the regeneration of lost body parts in planaria and amphibians, it is interesting to speculate whether an evolutionarily conserved regenerative mechanism exists. Of course, the formation of blastema involves several tissue types of different origins, which is different from one or two epithelial cell types in adult liver regeneration.

Our data showed that hepatocyte reprogramming is strongly associated with dynamic immune responses. Notably, periportal KCs are the major cellular components producing IL-6 as a specialized reprogramming niche signal for proximate hepatocytes (Figure S6F). Macrophages have been reported to perform a plethora of functions in injured tissues.[18,19] Nevertheless, it is surprising that macrophages also function as key niche cells controlling reprogramming, highlighting their master role in tissue repair and regeneration. In contrast, bone-marrow-derived MoMFs are not involved in, which functionally distinguishes resident KCs and MoMFs from the circulation. We also wish to note that IL-6-secreting KCs locate in specific regions, which are 1–5 layers away from injured bile ducts. The location of these IL-6-secreting KCs are only partially overlapped with the injured area. The specialized regional activation of KCs may be induced by DDC directly or by local metabolites, proinflammatory factors and DAMPs released from injured hepatocytes and cholangiocytes.[19] It would be interesting to characterize underlying mechanisms and factors in the future. Moreover, it was unexpected that a single proinflammatory factor, IL-6, would possess the prominent ability to trigger highly efficient *in vivo* reprogramming. This is in sharp contrast to those designed for *in vitro* reprogramming that use cocktails of multiple factors and have relatively low efficiencies. Interestingly, several studies around 20 years ago have also shown that IL-6 protects hepatocytes from injuries.[36,37] However, the underlying mechanisms remained unclear at the time. Our data suggest that the protective function of IL-6 is likely dependent on its regulation of hepatocyte reprogramming.

We demonstrated that STAT3 is a major downstream effector that mediates IL-6-induced hepatocyte reprogramming. A

(C) Integrative Genomics Viewer (IGV) plot showed the ChIP-seq peaks of STAT3 and input on *Sox9-site* and *Spp1-site*.
(D) Heatmap of STAT3-binding signals in RRGs. ATAC-seq signals of *Arid1a*$^{\Delta li}$ hepatocytes and DDC-induced LPLCs were shown in the same sites with STAT3-binding sites in RRGs.
(E) Quantification of ATAC-seq signals in STAT3-binding RRGs sites in *Arid1a*$^{\Delta li}$ hepatocytes and LPLC.s.
(F) Schematic view showed HDTVi of IL-6 in *Arid1a*$^{f/f}$ and *Arid1a*$^{\Delta li}$ mice. Immunofluorescent staining of SOX9 was shown (n = 3).
(G) IGV plot showed STAT3 and H3K27ac ChIP-seq peaks on *Sox9-site* and *Spp1-site* in Figure 6C.
(H) Reporter vectors (*Sox9-site-mCherry* or *Spp1-site-pHSVtk-mCherry*) were co-transfected with IL-6 into the *Stat3*$^{f/f}$ and *Stat3*$^{\Delta li}$ livers by HDTVi. *mCherry* expression in the liver was measured by qRT-PCR.
(I) Heatmap of H3K27ac ChIP-seq signals in STAT3-binding RRGs in E12.5 hepatoblasts and LPLCs.
(J) Average H3K27ac signals on Group 1 and Group 2 sites.
(K) Distribution of STAT3-binding peaks on Group 1 and Group 2 sites was shown. Proximal peaks and distal peaks were annotated based on the distance from TSS.
Scale bars: 100 μm. Data were presented as mean ± SD; *$p < 0.05$, **$p < 0.01$, t test. See also Figure S6.

remarkable feature of regeneration is the activation of genes that are critical in embryogenesis, and it is often questionable whether gene expression programs in regeneration share regulations with those in development. Intriguingly, our findings demonstrate that STAT3, a transcription factor not involved in hepatocyte lineage specification, re-activates almost the entire set of RRGs. Moreover, STAT3-binding enhancers of RRGs showed active H3K27ac modifications specific for liver injury and repair. These data illustrate an injury-responsive, regeneration-specific transcriptional mechanism by which the reprogramming of differentiated cells in other tissues might follow.

Repurposing the proinflammatory IL-6/STAT3 for the expression of progenitor programs and hepatocyte dedifferentiation renews the understanding of the role of IL-6/STAT3 signaling in tissue injury and repair. Our findings may provide not only a framework to understand tissue repair, but also supply a potential strategy to develop treatments for repair-related liver diseases by unlocking the expression of RRGs. For example, it would be worth testing IC7Fc,[38] an engineered IL-6-like protein that specifically elicits STAT3 activation in hepatocytes without the signs of inflammatory activation in immune cells, for promoting liver regeneration.

Limitations of the study

In this study, periportal liver injury models were implemented to demonstrate the repurposed function of KCs and the proinflammatory IL-6/STAT3 signaling in hepatocyte reprogramming. It will be interesting to determine whether the process is similarly regulated in other forms of liver injuries, such as pericentral liver injury and partial hepatectomy. By analyzing the expression of *Sox9* and RRGs in published scRNA-seq data,[39] we found that it was likely that hepatocyte reprogramming might occur in acetaminophen (APAP)-induced pericentral liver injury (Figures S6G and S6H). Furthermore, our preliminary data showed that APAP induced the formation of $SOX9^{+}HNF4\alpha^{+}$ hepatocytes at multiple time points, which were also positive for STAT3 staining (Figures S6I–S6N). It is worth to test whether similar regulatory mechanisms of hepatocyte reprogramming may be involved in other injuries.

STAR★METHODS

Detailed methods are provided in the online version of this paper and include the following:

SUPPLEMENTAL INFORMATION

Supplemental information can be found online at https://doi.org/10.1016/j.stem.2023.01.009.

ACKNOWLEDGMENTS

We thank Fuchou Tang (Peking University, China) and Yun Gao (Peking University, China) for help with Smart-seq2 experiments. We thank Yi Arial Zeng (CEMCS, CAS, China), Hongyan Wang (CEMCS, CAS, China), Jing Wang (Shanghai Institute of Immunology, China), Dangsheng Li (CEMCS, CAS, China), Ting Chen (National Institute of Biological Sciences, China), and Bing Gao (National Institutes of Health, USA) for critical comments and suggestions. We also thank the core facilities at CEMCS. This project was supported by the National Key Research and Development Project (2019YFA0801503), the National Natural Science Foundation of China (NSFC) (31930030), the National Key Research and Development Project (2019YFA0802001, 2021YFF1200902), the "Strategic Priority Research Program" of the Chinese Academy of Sciences (CAS, XDA16020201), the National Natural Science Foundation of China (91942313, 92168202, 32221002, T2122018), Shanghai Science and Technology Committee (22JC1403000), Shanghai Municipal Science and Technology Major Project, CAS Youth Innovation Promotion Association (2018307), and the Shanghai Sailing Program (22YF1458000).

AUTHOR CONTRIBUTIONS

L.L., L.C., and L.H. designed the study. L.L. and L.C. performed most of the experiments. P.L. performed bioinformatic analysis. L.C., Y.M., W.Z., and L.L. performed scRNA-seq experiments. Z.L. performed monocyte/MoMF lineage tracing experiments. S.B. performed the low-cell number RNA-seq experiments. Xiaolong Ma performed bioinformatic analysis of ChIP-seq. L.L., L.C., H.N., and J.C. performed mouse experiments. Y.L., H.L., F.G., Y.N., L.J., and Xiong Ma provided intellectual input and experimental design. L.L., L.C., P.L., and L.H. analyzed the data and wrote the manuscript.

DECLARATION OF INTERESTS

The authors declare no competing interests.

Received: August 19, 2022
Revised: December 12, 2022
Accepted: January 20, 2023
Published: February 13, 2023

REFERENCES

1. Wells, J.M., and Watt, F.M. (2018). Diverse mechanisms for endogenous regeneration and repair in mammalian organs. Nature *557*, 322–328. https://doi.org/10.1038/s41586-018-0073-7.
2. Jain, R., Barkauskas, C.E., Takeda, N., Bowie, E.J., Aghajanian, H., Wang, Q., Padmanabhan, A., Manderfield, L.J., Gupta, M., Li, D., et al. (2015). Plasticity of Hopx(+) type I alveolar cells to regenerate type II cells in the lung. Nat. Commun. *6*, 6727. https://doi.org/10.1038/ncomms7727.
3. Tetteh, P.W., Basak, O., Farin, H.F., Wiebrands, K., Kretzschmar, K., Begthel, H., van den Born, M., Korving, J., de Sauvage, F., van Es, J.H., et al. (2016). Replacement of lost Lgr5-positive stem cells through plasticity of their enterocyte-lineage daughters. Cell Stem Cell *18*, 203–213. https://doi.org/10.1016/j.stem.2016.01.001.
4. Chera, S., Baronnier, D., Ghila, L., Cigliola, V., Jensen, J.N., Gu, G., Furuyama, K., Thorel, F., Gribble, F.M., Reimann, F., and Herrera, P.L. (2014). Diabetes recovery by age-dependent conversion of pancreatic delta-cells into insulin producers. Nature *514*, 503–507. https://doi.org/10.1038/nature13633.
5. Raven, A., Lu, W.Y., Man, T.Y., Ferreira-Gonzalez, S., O'Duibhir, E., Dwyer, B.J., Thomson, J.P., Meehan, R.R., Bogorad, R., Koteliansky, V., et al. (2017). Cholangiocytes act as facultative liver stem cells during impaired hepatocyte regeneration. Nature *547*, 350–354. https://doi.org/10.1038/nature23015.
6. Schaub, J.R., Huppert, K.A., Kurial, S.N.T., Hsu, B.Y., Cast, A.E., Donnelly, B., Karns, R.A., Chen, F., Rezvani, M., Luu, H.Y., et al. (2018). De novo formation of the biliary system by TGFbeta-mediated hepatocyte transdifferentiation. Nature *557*, 247–251. https://doi.org/10.1038/s41586-018-0075-5.
7. Tarlow, B.D., Pelz, C., Naugler, W.E., Wakefield, L., Wilson, E.M., Finegold, M.J., and Grompe, M. (2014). Bipotential adult liver progenitors are derived from chronically injured mature hepatocytes. Cell Stem Cell *15*, 605–618. https://doi.org/10.1016/j.stem.2014.09.008.
8. Li, W., Yang, L., He, Q., Hu, C., Zhu, L., Ma, X., Ma, X., Bao, S., Li, L., Chen, Y., et al. (2019). A homeostatic Arid1a-dependent permissive chromatin state licenses hepatocyte responsiveness to liver-injury-associated YAP signaling. Cell Stem Cell *25*, 54–68.e5. https://doi.org/10.1016/j.stem.2019.06.008.
9. Yanger, K., Zong, Y., Maggs, L.R., Shapira, S.N., Maddipati, R., Aiello, N.M., Thung, S.N., Wells, R.G., Greenbaum, L.E., and Stanger, B.Z. (2013). Robust cellular reprogramming occurs spontaneously during liver regeneration. Genes Dev. *27*, 719–724. https://doi.org/10.1101/gad.207803.112.
10. Russell, J.O., and Monga, S.P. (2018). Wnt/beta-catenin signaling in liver development, homeostasis, and pathobiology. Annu. Rev. Pathol. *13*, 351–378. https://doi.org/10.1146/annurev-pathol-020117-044010.
11. Merrell, A.J., and Stanger, B.Z. (2016). Adult cell plasticity in vivo: de-differentiation and transdifferentiation are back in style. Nat. Rev. Mol. Cell Biol. *17*, 413–425. https://doi.org/10.1038/nrm.2016.24.
12. Yimlamai, D., Christodoulou, C., Galli, G.G., Yanger, K., Pepe-Mooney, B., Gurung, B., Shrestha, K., Cahan, P., Stanger, B.Z., and Camargo, F.D. (2014). Hippo pathway activity influences liver cell fate. Cell *157*, 1324–1338. https://doi.org/10.1016/j.cell.2014.03.060.
13. Tanimizu, N., Nishikawa, Y., Ichinohe, N., Akiyama, H., and Mitaka, T. (2014). Sry HMG box protein 9-positive (Sox9+) epithelial cell adhesion molecule-negative (EpCAM-) biphenotypic cells derived from hepatocytes are involved in mouse liver regeneration. J. Biol. Chem. *289*, 7589–7598. https://doi.org/10.1074/jbc.M113.517243.
14. Takahashi, K., and Yamanaka, S. (2006). Induction of pluripotent stem cells from mouse embryonic and adult fibroblast cultures by defined factors. Cell *126*, 663–676. https://doi.org/10.1016/j.cell.2006.07.024.
15. Huang, P., He, Z., Ji, S., Sun, H., Xiang, D., Liu, C., Hu, Y., Wang, X., and Hui, L. (2011). Induction of functional hepatocyte-like cells from mouse fibroblasts by defined factors. Nature *475*, 386–389. https://doi.org/10.1038/nature10116.
16. Goldman, J.A., and Poss, K.D. (2020). Gene regulatory programmes of tissue regeneration. Nat. Rev. Genet. *21*, 511–525. https://doi.org/10.1038/s41576-020-0239-7.
17. Machado, L., Geara, P., Camps, J., Dos Santos, M., Teixeira-Clerc, F., Van Herck, J., Varet, H., Legendre, R., Pawlotsky, J.M., Sampaolesi, M., et al. (2021). Tissue damage induces a conserved stress response that initiates quiescent muscle stem cell activation. Cell Stem Cell *28*, 1125–1135.e7. https://doi.org/10.1016/j.stem.2021.01.017.
18. Blériot, C., and Ginhoux, F. (2019). Understanding the heterogeneity of resident liver macrophages. Front. Immunol. *10*, 2694. https://doi.org/10.3389/fimmu.2019.02694.
19. Krenkel, O., and Tacke, F. (2017). Liver macrophages in tissue homeostasis and disease. Nat. Rev. Immunol. *17*, 306–321. https://doi.org/10.1038/nri.2017.11.
20. Seidman, J.S., Troutman, T.D., Sakai, M., Gola, A., Spann, N.J., Bennett, H., Bruni, C.M., Ouyang, Z., Li, R.Z., Sun, X., et al. (2020). Niche-specific reprogramming of epigenetic landscapes drives myeloid cell diversity in nonalcoholic steatohepatitis. Immunity *52*, 1057–1074.e7. https://doi.org/10.1016/j.immuni.2020.04.001.
21. Remmerie, A., Martens, L., Thoné, T., Castoldi, A., Seurinck, R., Pavie, B., Roels, J., Vanneste, B., De Prijck, S., Vanhockerhout, M., et al. (2020). Osteopontin expression identifies a subset of recruited macrophages distinct from Kupffer cells in the fatty liver. Immunity *53*, 641–657.e14. https://doi.org/10.1016/j.immuni.2020.08.004.
22. Mossanen, J.C., Krenkel, O., Ergen, C., Govaere, O., Liepelt, A., Puengel, T., Heymann, F., Kalthoff, S., Lefebvre, E., Eulberg, D., et al. (2016). Chemokine (C-C motif) receptor 2-positive monocytes aggravate the early phase of acetaminophen-induced acute liver injury. Hepatology *64*, 1667–1682. https://doi.org/10.1002/hep.28682.
23. Murakami, M., Kamimura, D., and Hirano, T. (2019). Pleiotropy and specificity: insights from the interleukin 6 family of cytokines. Immunity *50*, 812–831. https://doi.org/10.1016/j.immuni.2019.03.027.
24. Duncan, E.M., and Sánchez Alvarado, A. (2019). Regulation of genomic output and (pluri)potency in regeneration. Annu. Rev. Genet. *53*, 327–346. https://doi.org/10.1146/annurev-genet-112618-043733.
25. Kang, J., Hu, J., Karra, R., Dickson, A.L., Tornini, V.A., Nachtrab, G., Gemberling, M., Goldman, J.A., Black, B.L., and Poss, K.D. (2016). Modulation of tissue repair by regeneration enhancer elements. Nature *532*, 201–206. https://doi.org/10.1038/nature17644.
26. Wang, W., Hu, C.K., Zeng, A., Alegre, D., Hu, D., Gotting, K., Ortega Granillo, A., Wang, Y., Robb, S., Schnittker, R., et al. (2020). Changes in regeneration-responsive enhancers shape regenerative capacities in vertebrates. Science *369*, eaaz3090. https://doi.org/10.1126/science.aaz3090.
27. Harris, R.E., Stinchfield, M.J., Nystrom, S.L., McKay, D.J., and Hariharan, I.K. (2020). Damage-responsive, maturity-silenced enhancers regulate multiple genes that direct regeneration in Drosophila. Elife *9*, e58305. https://doi.org/10.7554/eLife.58305.
28. Guenther, C.A., Wang, Z., Li, E., Tran, M.C., Logan, C.Y., Nusse, R., Pantalena-Filho, L., Yang, G.P., and Kingsley, D.M. (2015). A distinct regulatory region of the Bmp5 locus activates gene expression following adult bone fracture or soft tissue injury. Bone *77*, 31–41. https://doi.org/10.1016/j.bone.2015.04.010.
29. Goldman, J.A., Kuzu, G., Lee, N., Karasik, J., Gemberling, M., Foglia, M.J., Karra, R., Dickson, A.L., Sun, F., Tolstorukov, M.Y., and Poss, K.D. (2017). Resolving heart regeneration by replacement histone profiling. Dev. Cell *40*, 392–404.e5. https://doi.org/10.1016/j.devcel.2017.01.013.
30. Harris, R.E., Setiawan, L., Saul, J., and Hariharan, I.K. (2016). Localized epigenetic silencing of a damage-activated WNT enhancer limits regeneration in mature Drosophila imaginal discs. Elife *5*, e11588. https://doi.org/10.7554/eLife.11588.
31. Lee, J.W., Stone, M.L., Porrett, P.M., Thomas, S.K., Komar, C.A., Li, J.H., Delman, D., Graham, K., Gladney, W.L., Hua, X., et al. (2019). Hepatocytes direct the formation of a pro-metastatic niche in the liver. Nature *567*, 249–252. https://doi.org/10.1038/s41586-019-1004-y.

32. Goldstein, I., Paakinaho, V., Baek, S., Sung, M.H., and Hager, G.L. (2017). Synergistic gene expression during the acute phase response is characterized by transcription factor assisted loading. Nat. Commun. *8*, 1849. https://doi.org/10.1038/s41467-017-02055-5.

33. Haga, S., Ogawa, W., Inoue, H., Terui, K., Ogino, T., Igarashi, R., Takeda, K., Akira, S., Enosawa, S., Furukawa, H., et al. (2005). Compensatory recovery of liver mass by Akt-mediated hepatocellular hypertrophy in liver-specific STAT3-deficient mice. J. Hepatol. *43*, 799–807. https://doi.org/10.1016/j.jhep.2005.03.027.

34. Rada-Iglesias, A., Bajpai, R., Swigut, T., Brugmann, S.A., Flynn, R.A., and Wysocka, J. (2011). A unique chromatin signature uncovers early developmental enhancers in humans. Nature *470*, 279–283. https://doi.org/10.1038/nature09692.

35. Karin, M., and Clevers, H. (2016). Reparative inflammation takes charge of tissue regeneration. Nature *529*, 307–315. https://doi.org/10.1038/nature17039.

36. Cressman, D.E., Greenbaum, L.E., DeAngelis, R.A., Ciliberto, G., Furth, E.E., Poli, V., and Taub, R. (1996). Liver failure and defective hepatocyte regeneration in interleukin-6-deficient mice. Science *274*, 1379–1383. https://doi.org/10.1126/science.274.5291.1379.

37. Kovalovich, K., DeAngelis, R.A., Li, W., Furth, E.E., Ciliberto, G., and Taub, R. (2000). Increased toxin-induced liver injury and fibrosis in interleukin-6-deficient mice. Hepatology *31*, 149–159. https://doi.org/10.1002/hep.510310123.

38. Findeisen, M., Allen, T.L., Henstridge, D.C., Kammoun, H., Brandon, A.E., Baggio, L.L., Watt, K.I., Pal, M., Cron, L., Estevez, E., et al. (2019). Treatment of type 2 diabetes with the designer cytokine IC7Fc. Nature *574*, 63–68. https://doi.org/10.1038/s41586-019-1601-9.

39. Ben-Moshe, S., Veg, T., Manco, R., Dan, S., Papinutti, D., Lifshitz, A., Kolodziejczyk, A.A., Bahar Halpern, K., Elinav, E., and Itzkovitz, S. (2022). The spatiotemporal program of zonal liver regeneration following acute injury. Cell Stem Cell *29*, 973–989.e10. https://doi.org/10.1016/j.stem.2022.04.008.

40. Pepe-Mooney, B.J., Dill, M.T., Alemany, A., Ordovas-Montanes, J., Matsushita, Y., Rao, A., Sen, A., Miyazaki, M., Anakk, S., Dawson, P.A., et al. (2019). Single-cell analysis of the liver epithelium reveals dynamic heterogeneity and an essential role for YAP in homeostasis and regeneration. Cell Stem Cell *25*, 23–38.e8. https://doi.org/10.1016/j.stem.2019.04.004.

41. Postic, C., and Magnuson, M.A. (2000). DNA excision in liver by an albumin-Cre transgene occurs progressively with age. Genesis *26*, 149–150. https://doi.org/10.1002/(sici)1526-968x(200002)26:2<149::aid-gene16>3.0.co;2-v.

42. Gao, X., Tate, P., Hu, P., Tjian, R., Skarnes, W.C., and Wang, Z. (2008). ES cell pluripotency and germ-layer formation require the SWI/SNF chromatin remodeling component BAF250a. Proc. Natl. Acad. Sci. USA *105*, 6656–6661. https://doi.org/10.1073/pnas.0801802105.

43. Li, Y., Feng, J., Song, S., Li, H., Yang, H., Zhou, B., Li, Y., Yue, Z., Lian, H., Liu, L., et al. (2020). gp130 controls cardiomyocyte proliferation and heart regeneration. Circulation *142*, 967–982. https://doi.org/10.1161/CIRCULATIONAHA.119.044484.

44. Zhang, N., Bai, H., David, K.K., Dong, J., Zheng, Y., Cai, J., Giovannini, M., Liu, P., Anders, R.A., and Pan, D. (2010). The Merlin/NF2 tumor suppressor functions through the YAP oncoprotein to regulate tissue homeostasis in mammals. Dev. Cell *19*, 27–38. https://doi.org/10.1016/j.devcel.2010.06.015.

45. Shinkai, Y., Rathbun, G., Lam, K.P., Oltz, E.M., Stewart, V., Mendelsohn, M., Charron, J., Datta, M., Young, F., and Stall, A.M. (1992). RAG-2-deficient mice lack mature lymphocytes owing to inability to initiate V(D)J rearrangement. Cell *68*, 855–867. https://doi.org/10.1016/0092-8674(92)90029-c.

46. Shultz, L.D., Lyons, B.L., Burzenski, L.M., Gott, B., Chen, X., Chaleff, S., Kotb, M., Gillies, S.D., King, M., Mangada, J., et al. (2005). Human lymphoid and myeloid cell development in NOD/LtSz-scid IL2R gamma null mice engrafted with mobilized human hemopoietic stem cells. J. Immunol. *174*, 6477–6489. https://doi.org/10.4049/jimmunol.174.10.6477.

47. Liu, Z., Gu, Y., Chakarov, S., Bleriot, C., Kwok, I., Chen, X., Shin, A., Huang, W., Dress, R.J., Dutertre, C.A., et al. (2019). Fate mapping via Ms4a3-expression history traces monocyte-derived cells. Cell *178*, 1509–1525.e19. https://doi.org/10.1016/j.cell.2019.08.009.

48. Martin, M. (2011). Cutadapt removes adapter sequences from high-throughput sequencing reads. EMBnet. j. *17*, 3. https://doi.org/10.14806/ej.17.1.200.

49. Bolger, A.M., Lohse, M., and Usadel, B. (2014). Trimmomatic: a flexible trimmer for Illumina sequence data. Bioinformatics *30*, 2114–2120. https://doi.org/10.1093/bioinformatics/btu170.

50. Smith, T., Heger, A., and Sudbery, I. (2017). UMI-tools: modeling sequencing errors in unique molecular identifiers to improve quantification accuracy. Genome Res. *27*, 491–499. https://doi.org/10.1101/gr.209601.116.

51. Dobin, A., Davis, C.A., Schlesinger, F., Drenkow, J., Zaleski, C., Jha, S., Batut, P., Chaisson, M., and Gingeras, T.R. (2013). STAR: ultrafast universal RNA-seq aligner. Bioinformatics *29*, 15–21. https://doi.org/10.1093/bioinformatics/bts635.

52. Anders, S., Pyl, P.T., and Huber, W. (2015). HTSeq–a Python framework to work with high-throughput sequencing data. Bioinformatics *31*, 166–169. https://doi.org/10.1093/bioinformatics/btu638.

53. Stuart, T., Butler, A., Hoffman, P., Hafemeister, C., Papalexi, E., Mauck, W.M., 3rd, Hao, Y., Stoeckius, M., Smibert, P., and Satija, R. (2019). Comprehensive integration of single-cell data. Cell *177*, 1888–1902.e21. https://doi.org/10.1016/j.cell.2019.05.031.

54. Cao, J., Spielmann, M., Qiu, X., Huang, X., Ibrahim, D.M., Hill, A.J., Zhang, F., Mundlos, S., Christiansen, L., Steemers, F.J., et al. (2019). The single-cell transcriptional landscape of mammalian organogenesis. Nature *566*, 496–502. https://doi.org/10.1038/s41586-019-0969-x.

55. Subramanian, A., Tamayo, P., Mootha, V.K., Mukherjee, S., Ebert, B.L., Gillette, M.A., Paulovich, A., Pomeroy, S.L., Golub, T.R., Lander, E.S., and Mesirov, J.P. (2005). Gene set enrichment analysis: a knowledge-based approach for interpreting genome-wide expression profiles. Proc. Natl. Acad. Sci. USA *102*, 15545–15550. https://doi.org/10.1073/pnas.0506580102.

56. Hänzelmann, S., Castelo, R., and Guinney, J. (2013). GSVA: gene set variation analysis for microarray and RNA-seq data. BMC Bioinformatics *14*, 7. https://doi.org/10.1186/1471-2105-14-7.

57. Ritchie, M.E., Phipson, B., Wu, D., Hu, Y., Law, C.W., Shi, W., and Smyth, G.K. (2015). limma powers differential expression analyses for RNA-sequencing and microarray studies. Nucleic Acids Res. *43*, e47. https://doi.org/10.1093/nar/gkv007.

58. Love, M.I., Huber, W., and Anders, S. (2014). Moderated estimation of fold change and dispersion for RNA-seq data with DESeq2. Genome Biol. *15*, 550. https://doi.org/10.1186/s13059-014-0550-8.

59. Yu, G., Wang, L.G., Han, Y., and He, Q.Y. (2012). clusterProfiler: an R package for comparing biological themes among gene clusters. Omics *16*, 284–287. https://doi.org/10.1089/omi.2011.0118.

60. Langmead, B., and Salzberg, S.L. (2012). Fast gapped-read alignment with Bowtie 2. Nat. Methods *9*, 357–359. https://doi.org/10.1038/nmeth.1923.

61. Zhang, Y., Liu, T., Meyer, C.A., Eeckhoute, J., Johnson, D.S., Bernstein, B.E., Nusbaum, C., Myers, R.M., Brown, M., Li, W., and Liu, X.S. (2008). Model-based analysis of ChIP-Seq (MACS). Genome Biol. *9*, R137. https://doi.org/10.1186/gb-2008-9-9-r137.

62. Ramírez, F., Ryan, D.P., Grüning, B., Bhardwaj, V., Kilpert, F., Richter, A.S., Heyne, S., Dündar, F., and Manke, T. (2016). deepTools2: a next generation web server for deep-sequencing data analysis. Nucleic Acids Res. *44*, W160–W165. https://doi.org/10.1093/nar/gkw257.

63. Robinson, J.T., Thorvaldsdóttir, H., Winckler, W., Guttman, M., Lander, E.S., Getz, G., and Mesirov, J.P. (2011). Integrative genomics viewer. Nat. Biotechnol. *29*, 24–26. https://doi.org/10.1038/nbt.1754.

64. McLean, C.Y., Bristor, D., Hiller, M., Clarke, S.L., Schaar, B.T., Lowe, C.B., Wenger, A.M., and Bejerano, G. (2010). GREAT improves functional interpretation of cis-regulatory regions. Nat. Biotechnol. *28*, 495–501. https://doi.org/10.1038/nbt.1630.

65. Moh, A., Iwamoto, Y., Chai, G.X., Zhang, S.S., Kano, A., Yang, D.D., Zhang, W., Wang, J., Jacoby, J.J., Gao, B., et al. (2007). Role of STAT3 in liver regeneration: survival, DNA synthesis, inflammatory reaction and liver mass recovery. Lab. Invest. *87*, 1018–1028. https://doi.org/10.1038/labinvest.3700630.

66. Fleming, T.J., Fleming, M.L., and Malek, T.R. (1993). Selective expression of Ly-6G on myeloid lineage cells in mouse bone marrow. RB6-8C5 mAb to granulocyte-differentiation antigen (Gr-1) detects members of the Ly-6 family. J. Immunol. *151*, 2399–2408.

67. van Rooijen, N., Sanders, A., and van den Berg, T.K. (1996). Apoptosis of macrophages induced by liposome-mediated intracellular delivery of clodronate and propamidine. J. Immunol. Methods *193*, 93–99. https://doi.org/10.1016/0022-1759(96)00056-7.

68. Sakai, M., Troutman, T.D., Seidman, J.S., Ouyang, Z., Spann, N.J., Abe, Y., Ego, K.M., Bruni, C.M., Deng, Z., Schlachetzki, J.C.M., et al. (2019). Liver-derived signals sequentially reprogram myeloid enhancers to initiate and maintain Kupffer cell identity. Immunity *51*, 655–670.e8. https://doi.org/10.1016/j.immuni.2019.09.002.

69. Liu, F., Song, Y., and Liu, D. (1999). Hydrodynamics-based transfection in animals by systemic administration of plasmid DNA. Gene Ther. *6*, 1258–1266. https://doi.org/10.1038/sj.gt.3300947.

70. Li, D., Fu, J., Du, M., Zhang, H., Li, L., Cen, J., Li, W., Chen, X., Lin, Y., Conway, E.M., et al. (2016). Hepatocellular carcinoma repression by TNFalpha-mediated synergistic lethal effect of mitosis defect-induced senescence and cell death sensitization. Hepatology *64*, 1105–1120. https://doi.org/10.1002/hep.28637.

71. Dorrell, C., Erker, L., Lanxon-Cookson, K.M., Abraham, S.L., Victoroff, T., Ro, S., Canaday, P.S., Streeter, P.R., and Grompe, M. (2008). Surface markers for the murine oval cell response. Hepatology *48*, 1282–1291. https://doi.org/10.1002/hep.22468.

72. Tarlow, B.D., Finegold, M.J., and Grompe, M. (2014). Clonal tracing of Sox9+ liver progenitors in mouse oval cell injury. Hepatology *60*, 278–289. https://doi.org/10.1002/hep.27084.

73. Chen, J., Suo, S., Tam, P.P., Han, J.J., Peng, G., and Jing, N. (2017). Spatial transcriptomic analysis of cryosectioned tissue samples with Geo-seq. Nat. Protoc. *12*, 566–580. https://doi.org/10.1038/nprot.2017.003.

74. Picelli, S., Björklund, Å.K., Faridani, O.R., Sagasser, S., Winberg, G., and Sandberg, R. (2013). Smart-seq2 for sensitive full-length transcriptome profiling in single cells. Nat. Methods *10*, 1096–1098. https://doi.org/10.1038/nmeth.2639.

75. Picelli, S., Faridani, O.R., Björklund, A.K., Winberg, G., Sagasser, S., and Sandberg, R. (2014). Full-length RNA-seq from single cells using Smart-seq2. Nat. Protoc. *9*, 171–181. https://doi.org/10.1038/nprot.2014.006.

76. Li, L., Dong, J., Yan, L., Yong, J., Liu, X., Hu, Y., Fan, X., Wu, X., Guo, H., Wang, X., et al. (2017). Single-cell RNA-seq analysis maps development of human germline cells and gonadal niche interactions. Cell Stem Cell *20*, 858–873.e4. https://doi.org/10.1016/j.stem.2017.03.007.

77. Islam, S., Zeisel, A., Joost, S., La Manno, G., Zajac, P., Kasper, M., Lönnerberg, P., and Linnarsson, S. (2014). Quantitative single-cell RNA-seq with unique molecular identifiers. Nat. Methods *11*, 163–166. https://doi.org/10.1038/nmeth.2772.

78. Satija, R., Farrell, J.A., Gennert, D., Schier, A.F., and Regev, A. (2015). Spatial reconstruction of single-cell gene expression data. Nat. Biotechnol. *33*, 495–502. https://doi.org/10.1038/nbt.3192.

79. Trapnell, C., Cacchiarelli, D., Grimsby, J., Pokharel, P., Li, S., Morse, M., Lennon, N.J., Livak, K.J., Mikkelsen, T.S., and Rinn, J.L. (2014). The dynamics and regulators of cell fate decisions are revealed by pseudotemporal ordering of single cells. Nat. Biotechnol. *32*, 381–386. https://doi.org/10.1038/nbt.2859.

Please cite this article in press as: Li et al., Kupffer-cell-derived IL-6 is repurposed for hepatocyte dedifferentiation via activating progenitor genes from injury-specific enhancers, Cell Stem Cell (2023), https://doi.org/10.1016/j.stem.2023.01.009

STAR★METHODS

KEY RESOURCES TABLE

REAGENT or RESOURCE	SOURCE	IDENTIFIER
Antibodies		
SOX9	Millipore	Cat# Ab5535; RRID: AB_2239761
OPN	R&D Systems	Cat# AF808; RRID: AB_2194992
HNF4α	Abcam	Cat# ab181604; RRID: N/A
GFP	Santa Cruz	Cat# sc-9996; RRID: AB_627695
Ki67	Abcam	Cat# ab15580; RRID: AB_443209
H3K27ac	Abcam	Cat# ab4729; RRID: AB_2118291
RFP	Rockland	Cat# 600-401-379; RRID: AB_2209751
YAP	Cell Signaling	Cat# 14074; RRID: AB_2650491
F4/80	Cell Signaling	Cat# 70076; RRID: AB_2799771
CLEC4F	R&D Systems	Cat# AF2784; RRID: AB_2081339
pSTAT3(Y705)	Cell Signaling	Cat# 9145; RRID: AB_2491009
TruStain FcX™ PLUS (anti-mouse CD16/32) Antibody	BioLegend	Cat# 156604; RRID: N/A
CD45 Monoclonal Antibody (I3/2.3), APC-Cyanine7	Thermo Fisher Scientific	Cat# A15395; RRID: AB_2534409
CD11b Monoclonal Antibody (M1/70), FITC	Thermo Fisher Scientific	Cat# 11-0112-82; RRID: AB_464935
CD11b Monoclonal Antibody (ICRF44), APC-eFluor™ 780	Thermo Fisher Scientific	Cat# 47-0118-41; RRID: AB_10717294
CD3e Monoclonal Antibody (145-2C11), APC	Thermo Fisher Scientific	Cat# 17-0031-82; RRID: AB_46931
CD19 Monoclonal Antibody (eBio1D3 (1D3)), APC	Thermo Fisher Scientific	Cat# 17-0193-82; RRID: AB_1659676
CD3e Monoclonal Antibody (145-2C11), PE	Thermo Fisher Scientific	Cat# 12-0031-81; RRID: AB_465495
NK1.1 Monoclonal Antibody (PK136), APC	Thermo Fisher Scientific	Cat# 17-5941-82; RRID: AB_469479
Alexa Fluor® 488 anti-mouse CD49b	Biolegend	Cat# 108913; RRID: AB_492879
TIM-4 Monoclonal Antibody (54 (RMT4-54)), PE	Thermo Fisher Scientific	Cat# 12-5866-82; RRID: AB_1257163
TIM-4	BD Biosciences	Cat# 742773; RRID: AB_2741037
F4/80 Monoclonal Antibody (BM8), PE	Thermo Fisher Scientific	Cat# 12-4801-82; RRID: AB_465923
F4/80 Monoclonal Antibody (BM8), APC	Thermo Fisher Scientific	Cat# 17-4801-80; RRID: AB_2784647
Brilliant Violet 421(TM) anti-mouse F4/80	BioLegend	Cat# 123137; RRID: AB_2563102
Ly-6C Monoclonal Antibody (HK1.4), PE-Cyanine7	Thermo Fisher Scientific	Cat# 25-5932-82; RRID: AB_2573503
Ly-6C Monoclonal Antibody (HK1.4), APC	Thermo Fisher Scientific	Cat# 17-5932-80; RRID: AB_1724155
Ly-6G Monoclonal Antibody (1A8-Ly6g), APC	Thermo Fisher Scientific	Cat# 17-9668-82; RRID: AB_2573307
IL-6 Monoclonal Antibody (MP5-20F3), PE	Thermo Fisher Scientific	Cat# 12-7061-82; RRID: AB_466165

(*Continued on next page*)

Continued

REAGENT or RESOURCE	SOURCE	IDENTIFIER
Rat IgG1 kappa Isotype Control (eBRG1), PE	Thermo Fisher Scientific	Cat# 12-4301-82; RRID: AB_470047
Normal Rabbit IgG	Cell Signaling	Cat# 2729P; RRID: N/A
F4/80 Monoclonal Antibody (BM8), Biotin	Thermo Fisher Scientific	Cat# 13-4801-82; RRID: AB_466657
TIM-4 Antibody, anti-mouse, Biotin, REAfinity™	Miltenyi Biotec	Cat# 130-116-642; RRID: AB_2733467
Alexa Fluor(R) 488 anti-mouse/ human Ki-67	BioLegend	Cat# 151204; RRID: AB_2566800
Anti-Ly6G antibody	Bio X Cell	Cat# BP0075-1; RRID: N/A
Rat IgG2a isotype	Bio X Cell	Cat# BP0089; RRID: N/A
Bacterial and virus strains		
AAV8.TBG.PI.Cre.rBG	Penn Vector Core	Addgene_107787
AAV8.TBG.PI.eGFP.WPRE.bGH	Penn Vector Core	Addgene_105535
Chemicals, peptides, and recombinant proteins		
DDC	Sigma-Aldrich	Cat# 137030
Dynabeads	Life Technologies	Cat# 10004D
SYBR® Premix Ex Taq™	Takara	Cat# rr420a
Proteinase K	Merck	Cat# 1245680100
Collagenase IV	Life Technologies	Cat# 17104019
Precision Count Beads	BioLegend	Cat# 424902
Brefeldin A	BioLegend	Cat# 420601
Guanidine isothiocyanate solution	Invitrogen	Cat# 15577-018
4,4'-Diaminodiphenylmethane	Tokyo Chemical Industry	Cat# M0220
4-Acetamidophenol	Adamas Reagent	Cat# 11969A
CLODRONATE LIPOSOMES & CONTROL LIPOSOMES (PBS)	LIPOSOMA	Cat# CP-005-005
Critical commercial assays		
Trueprep dna library prep kit	Vazyme Biotech	Cat# TD501
Trueprep index kit	Vazyme Biotech	Cat# TD202
MinElute PCR Purification Kit	QIAGEN	Cat# 28006
NEBNext® High-Fidelity 2X PCR Master Mix	NEB	Cat# M0541L
NEBNext Ultra DNA Library Prep Kit	NEB	Cat# E7370
Opal 4-Color Manual IHC Kit	Perkinelmer	Cat# NEL810001KT
SimpleChIP® Plus Sonication Chromatin IP Kit	CST	Cat# 56383
Intracellular Fixation & Permeabilization Buffer	Thermo Fisher Scientific	Cat# 88-8824-00
Foxp3 / Transcription Factor Fixation/Permeabilization Concentrate and Diluent	Thermo Fisher Scientific	Cat# 00-5521-00
Deposited data		
Raw and analyzed data	This paper	GSE193850
scRNA-seq dataset of DDC-injured hepatocytes	Pepe-Mooney et al.[40]	GSE125688
scRNA-seq dataset of APAP-injured hepatocytes	Ben-Moshe et al.[39]	https://itzkovitzapapp.weizmann.ac.il/apap/
ATAC-seq data of hepatocytes and LPLCs	Li et al.[8]	GSE111502

(*Continued on next page*)

Please cite this article in press as: Li et al., Kupffer-cell-derived IL-6 is repurposed for hepatocyte dedifferentiation via activating progenitor genes from injury-specific enhancers, Cell Stem Cell (2023), https://doi.org/10.1016/j.stem.2023.01.009

Continued

REAGENT or RESOURCE	SOURCE	IDENTIFIER
Experimental models: Organisms/strains		
Alb-Cre	Postic et al.[41]	N/A
Arid1a$^{f/f}$	Gao et al.[42]	N/A
gp130$^{f/f}$	Li et al.[43]	N/A
Yap$^{f/f}$	Zhang et al.[44]	N/A
Rag2$^{-/-}$	Shinkai et al.[45]	N/A
Il2rgc$^{-/-}$	Shultz et al.[46]	N/A
Ms4a3-Cre	Liu et al.[47]	N/A
Cx3cr1-GFP	Liu et al.[47]	N/A
Sox9-EGFP	MMRRC at University of California	MMRRC_011019-UCD
Il6ra$^{f/f}$	Gempharmatech Co., Ltd.	T009974
Il6$^{f/f}$	Gempharmatech Co., Ltd.	T005443
Clec4f-Cre-tdTomato	The Jackson Laboratory	033296
Rosa26-LSL-iDTR	The Jackson Laboratory	007900
Stat3$^{f/f}$	The Jackson Laboratory	016923
Ccr2$^{-/-}$	The Jackson Laboratory	004999
Rosa26-mTmG	The Jackson Laboratory	007676
Rosa26-LSL-tdTomato	The Jackson Laboratory	007905
Sox9-CreERT2	The Jackson Laboratory	018829
129S6/SvEvTac	Charles River Laboratories	N/A
Oligonucleotides		
Primers for qRT-PCR See Table S4	This paper	N/A
Recombinant DNA		
CMV-*GFP*	This paper	N/A
CMV-*Il6-P2A-GFP*	This paper	N/A
CMV-*Il1a-P2A-GFP*	This paper	N/A
CMV-*Il10-P2A-GFP*	This paper	N/A
CMV-*Il11-P2A-GFP*	This paper	N/A
CMV-*Cxcl1-P2A-GFP*	This paper	N/A
CMV-*Cxcl14-P2A-GFP*	This paper	N/A
CMV-*Il1b-P2A-GFP*	This paper	N/A
CMV-*Ccl2-P2A-GFP*	This paper	N/A
CMV-*Tnf-P2A-GFP*	This paper	N/A
CMV-*Csf1-P2A-GFP*	This paper	N/A
CMV-*Csf2-P2A-GFP*	This paper	N/A
CMV-*Csf3-P2A-GFP*	This paper	N/A
CMV-*Cxcl16-P2A-GFP*	This paper	N/A
CMV-*Wnt3a-P2A-GFP*	This paper	N/A
CMV-*Wnt4-P2A-GFP*	This paper	N/A
CMV-*Wnt7a-P2A-GFP*	This paper	N/A
Sox9-Site-mcherry	This paper	N/A
Spp1-Site-pHSVtk-mcherry	This paper	N/A
Software and algorithms		
Cell Ranger (v6.0.1)	10X Genomics	https://support.10xgenomics.com/single-cell-gene-expression/software/pipelines/latest/what-is-cell-ranger
Cutadapt (v1.14)	Martin.[48]	https://cutadapt.readthedocs.io/en/stable/
Trimmomatic	Bolger et al.[49]	https://github.com/usadellab/Trimmomatic
FASTX-Toolkit (v0.0.13)	N/A	http://hannonlab.cshl.edu/fastx_toolkit

(*Continued on next page*)

Continued

REAGENT or RESOURCE	SOURCE	IDENTIFIER
UMI-tools	Smith et al.[50]	https://github.com/CGATOxford/UMI-tools
STAR (v2.5.2b)	Dobin et al.[51]	https://github.com/alexdobin/STAR
Htseq-count (v0.6.0)	Anders et al.[52]	https://htseq.readthedocs.io/en/master/htseqcount.html
Seurat R package (v4.0.1)	Stuart et al.[53]	https://satijalab.org/seurat/
monocle3 R package (v1.0.0)	Cao et al.[54]	https://cole-trapnell-lab.github.io/monocle3
pheatmap R package (v.1.0.12)	N/A	https://rdrr.io/cran/pheatmap/
ggplot2 R package	N/A	https://ggplot2.tidyverse.org
Gene Set Enrichment Analysis (GSEA)	Subramanian et al.[55]	https://www.gsea-msigdb.org/gsea/index.jsp
GSVA R package (v1.38.2)	Hanzelmann et al.[56]	https://www.bioconductor.org/packages/release/bioc/html/GSVA.html
limma R package (v3.46.0)	Ritchie et al.[57]	https://www.bioconductor.org/packages/release/bioc/html/limma.html
DESeq2 R package	Love et al.[58]	https://bioconductor.org/packages/release/bioc/html/DESeq2.html
ClusterProfiler R package (v3.18.1)	Yu et al.[59]	https://bioconductor.org/packages/release/bioc/html/clusterProfiler.html
Bowtie2	Langmead et al.[60]	http://bowtie-bio.sourceforge.net/bowtie2/index.shtml
MACS (v2.1.1)	Zhang et al.[61]	https://macs3-project.github.io/MACS/
deepTools (v2.5.3)	Ramirez et al.[62]	https://deeptools.readthedocs.io/
Integrative Genomics Viewer (IGV)	Robinson et al.[63]	https://igv.org/
GREAT	McLean et al.[64]	http://bejerano.stanford.edu/great/public/html

RESOURCE AVAILABILITY

Lead contact

Further information and requests for resources and reagents should be directed to and will be fulfilled by the lead contact, Lijian Hui (huilab@sibcb.ac.cn).

Materials availability

All unique/stable reagents generated in this study are available from the Lead Contact without restriction.

Data and code availability

All sequencing data generated in the study have been deposited at Gene Expression Omnibus (GEO) and are publicly available as of the date of publication. Accession numbers are listed in the key resources table. This paper does not report original code. Any additional information required to reanalyze the data reported in this paper is available from the lead contact upon request.

EXPERIMENTAL MODEL AND SUBJECT DETAILS

Mice used in this study

Il6ra$^{f/f}$ mice (T009974) and *IL6*$^{f/f}$ mice (T005443) were purchased from Gempharmatech Co., Ltd. *Alb-Cre;Il6ra*$^{f/f}$ (*Il6ra*$^{\Delta li}$) and *Alb-Cre;Arid1a*$^{f/f}$ (*Arid1a*$^{\Delta li}$) mice were generated by crossing *Alb-Cre* mice[41] with *Il6ra*$^{f/f}$ mice and *Arid1a*$^{f/f}$ mice,[42] respectively. *Clec4f-Cre;Rosa26-LSL-iDTR* mice were generated by crossing *Clec4f-Cre-tdTomato* mice (Jax, 033296) with *Rosa26-LSL-iDTR* mice (Jax, 007900). *gp130*$^{f/f}$ mice[43] were generated and kindly provided by Y. Nie. *Stat3*$^{f/f}$ mice[65] (Jax, 016923) were kindly provided by L. Jiang. *Ccr2*$^{-/-}$ mice (Jax, 004999) were kindly provided by F. Ginhoux. *Rosa26-mTmG* mice (Jax, 007676) and all above mice were maintained on a mixed background (129S6/SvEvTac and C57BL/6J). *Yap*$^{f/f}$ mice[44] were on C57BL/6J genetic background. *Ms4a3-Cre;Rosa26-LSL-tdTomato;Cx3cr1-GFP* mice[47] was kindly provided by F. Ginhoux. *Sox9-EGFP* mice (RRID: MMRRC_011019-UCD) were purchased from MMRRC at University of California, Davis, and maintained on a mixed background (FVB/N and 129S6/SvEvTac). *Rag2*$^{-/-}$*;Il2rgc*$^{-/-}$ mice[45,46] were maintained on the Balb/c background. For macrophage depletion, neutrophil depletion, DAPM injury and APAP injury, 129S6/SvEvTac mice (Charles River Laboratories) were used unless otherwise specified. To identify the trigger factor of reprogramming, we used either 129S6/SvEvTac or FVB/N wild-type mice as recipients in HDTVi assays. IL-6-induced LPLCs were confirmed in both mouse lines. For HDTVi assays, *gp130*$^{f/f}$ mice, *Arid1a*$^{f/f}$ mice and *Stat3*$^{f/f}$ mice were maintained on the mixed genetic background of 129S6/SvEvTac and C57BL/6J, and *Yap*$^{f/f}$ mice were maintained on

Please cite this article in press as: Li et al., Kupffer-cell-derived IL-6 is repurposed for hepatocyte dedifferentiation via activating progenitor genes from injury-specific enhancers, Cell Stem Cell (2023), https://doi.org/10.1016/j.stem.2023.01.009

C57BL/6J genetic background. All mouse experiments were approved by the Institutional Animal Care and Use Committee of the Center for Excellence in Molecular Cell Science (CEMCS) and performed in accordance with this committee's guidelines. None of the mice used in these studies had been subjected to prior procedures and were drug and test naive. Mice were housed in a temperature- and light-controlled (12-h light/dark cycle) specific pathogen-free (SPF) animal facility, in individually ventilated cages always with companion mice. Mice used in this study were 8-12 weeks of age. Male mice were used for most of these mouse experiments.

Viral strains used in this study

Adeno-associated viruses 8 carrying Cre recombinase under the regulation of the thyroid hormone binding globulin promoter (AAV8.TBG.PI.Cre.rBG, AAV-Cre) and adeno-associated viruses 8 carrying green fluorescent protein under the regulation of the thyroid hormone binding globulin promoter (AAV8.TBG.PI.eGFP.WPRE.bGH, AAV-GFP) were purchased from University of Pennsylvania Vector Core. For AAV virus infection, 2.5×10^{11} genomic particles of AAV-Cre or AAV-GFP were reconstituted in 200 μL PBS and injected intravenously through tail veil injection with BD Ultra-Fine Insulin Syringes. After two weeks virus washing out, these mice then received DDC treatment or HDTVi of plasmids.

METHOD DETAILS

Liver injury induction and post-injury repair

For DDC-induced liver injury, mice were given 0.1% DDC (Sigma-Aldrich, 137030) diet (1 g per 1,000 g) for one week. For DAPM injury, mice were received one intraperitoneal injection of DAPM (Tokyo Chemical Industry, M0220) at a dose of 100 mg/kg body weight and were euthanized after one week. For APAP injury, mice were fasted for 12 hours prior to an intraperitoneal injection of acetaminophen (Adamas Reagent, 11969A) at a dose of 300 mg/kg body weight. For post-injury liver repair, mice were given 0.1% DDC diet for one or two weeks and then kept on normal diet for two days or one week.

Neutrophil, macrophage and KC depletion

Anti-Ly6G antibody 1A8[66] (Bio X Cell, BP0075-1) was used to deplete neutrophils in the liver. Neutrophil depletion was performed by intraperitoneal administration of 400 μg anti-Ly6G antibody 24 hours prior to injury induction. An additional of 200 μg antibody was administrated after three days of injury induction. Mice treated with rat IgG2a isotype control (Bio X Cell, BP0089) were used as control for neutrophil depletion.

Clodronate liposomes[67] were used to deplete macrophages in the liver. Macrophage depletion was performed by intravenous injection of clodronate liposomes (LIPOSOMA, CP-005-005) at a dose of 10 μL/g body weight 24 hours prior to injury induction. An additional injection was performed after three days of injury induction. Mice treated with PBS liposomes were used as control for clodronate liposomes treatment.

KC depletion was performed by intraperitoneal administration of 500 ng diphtheria toxin (Sigma) 24 hours prior to injury induction in *Clec4f-Cre;Rosa26-LSL-iDTR* mice.[68] Mice injected with PBS were used as control for KC depletion.

Hydrodynamic tail-vein injection

To overexpress genes in mouse hepatocytes, hydrodynamic tail-vein injection (HDTVi)[69] was used. The expression vector used in this experiment was pAAV with the cytomegalovirus immediate–early promoter (CMV) and GFP gene for expression of inserted complementary DNA (cDNA) shown in Figure 4A. Briefly, final concentration of plasmids at 0.5 μg/mL (in Figure 4B) or 5 μg/mL (in Figures 4C, 6A–6K, S4B, S4C, S5E, S5F, S5J, S5K, S5M, and S6A–S6C) was diluted in 0.9% NaCl solution. Mice were injected with the 0.9% NaCl solution/plasmid mix into the lateral tail vein with a total volume corresponding to 10% of body weight in 5-7 seconds. Plasmid DNA could be efficiently delivered into hepatocytes through the vena cava and central vein by relatively high-pressure tail vein injection. For bulk transcriptome analysis, IL-6 at 5 μg/mL were delivered into liver by HDTVi, which induced 98% of hepatocytes as $SOX9^{+}HNF4\alpha^{+}$ cells, from which all hepatocytes were isolated for transcriptome analysis.

Histology and immunostaining

For paraffin sections, liver samples were fixed in 4% PFA (4 °C) overnight and embedded in paraffin blocks next day. Immunohistochemistry staining and hematoxylin and eosin (H&E) staining were performed as previously described.[70]

For immunofluorescence, after antigen retrieved (AKOYA, NEL810001KT), paraffin sections (2 μm) were washed in TBST (0.1% Tween-80 in TBS) for 2 min, blocked in antibody diluent (AKOYA, NEL810001KT) for 1 hour at room temperature, and stained with primary antibody at 4 °C overnight. Primary antibodies included SOX9 (Millipore, Ab5535, 1:1000), OPN (R&D Systems, AF808, 1:1000), HNF4α (Abcam, ab181604, 1:1000), GFP (Santa Cruz, sc-9996, 1:200), RFP (Rockland, 600-401-379, 1:500), Ki67 (Abcam, ab15580, 1:1000), F4/80 (CST, 70076, 1:1000), CLEC4F (R&D Systems, AF2784, 1:1000), YAP (CST, 14074, 1:1000), pSTAT3 (CST, 9145, 1:100). Primary antibodies were detected using Opal™ 4-Color Manual IHC Kit (AKOYA, NEL810001KT) on paraffin sections according to the manufacturer's protocol. Sections were stained with DAPI (4',6-Diamidino-2-Phenylindole) and mounted with fluorescence mounting medium (Dako). Images were taken using an Olympus BX51 microscope or a confocal microscopy Leica TCS SP8 WLL. Images in different channels were merged by ImageJ software.

To describe the distribution and density of LPLCs and macrophages (KCs and MoMFs), fluorescent signals of LPLCs (SOX9$^+$ HNF4α^+), macrophages (F4/80$^+$), KCs (CLEC4F$^+$F4/80$^+$) and MoMFs (CLEC4F$^-$F4/80$^+$) were converted to digital signals using the 'spot' function in Imaris software. Position coordinates of each spot were analyzed by Two-Dimensional Kernel Density Estimation, and plotted via the 'ggplot2' package in R to quantify the cell distribution and density. To characterize the distribution of LPLCs and KCs across the liver lobule, the parenchymal area between one central vein to the most adjacent portal vein was equally divided into nine layers along the central-portal axis and the position of a cell in the lobule was determined by the relative distance to the portal vein and the central vein.

Blood biochemical analysis

Blood was collected and stored at 4 °C for one hour. Freshly isolated serum was obtained by centrifuging the blood at 12,000 g for 10 min and stored at -80 °C before use. ALP, TBA, ALT, AST, T-BIL, and blood glucose levels were detected according to the manufacturer's instructions (Shanghai Shensuo UNF Medical Diagnostic Articles Co., Ltd.). Activated partial thromboplastin time (APTT) was measured using an automated coagulation monitoring device (Teco, MC-4000, Germany) with a maximum recorded value of > 96 seconds.

The *in vivo* reporter assay

The *Sox9-site* was cloned from 2 kb upstream of ATG within STAT3-binding peak. The *Spp1-site* was cloned from 17 kb upstream of transcription start sites (TSS), i.e. the first distal STAT3-binding peak before TSS. *Sox9-site* and *Spp1-site* were then cloned into the front of a mCherry reporter vector. Plasmids of *Sox9-site-mcherry* and *Spp1-site-HSVtk promoter-mcherry* were efficiently transfected into mouse livers via HDTVi.

Flow cytometry, cell sorting and cell culture

All liver cells were isolated from normal or DDC-injured mouse livers by a modified two-step liver collagenase perfusion method. Perfused liver cells were filtered through a 70 μm filter (BD Bioscience). Non-parenchymal cells, including biliary epithelial cells, endothelial cells, hepatic stellate cells, macrophages, neutrophils and intrahepatic lymphocytes, were further purified by low speed gravity centrifugation (50 g × 1 min × 2) and medium speed gravity centrifugation (500 g × 5 min × 1) as previously described.[71] Antibody staining was carried out in FACS buffer for 30 min at 4 °C at the dilution of 1:200 after Fc blocking antibody (anti-CD16/CD32, BioLegend, 156604). Primary antibodies against CD45 (Thermo Fisher Scientific, A15395), CD11b (Thermo Fisher Scientific, 11-0112-82, 47-0118-41), CD3 (Thermo Fisher Scientific, 17-0031-82), CD19 (Thermo Fisher Scientific, 17-0193-82), NK1.1 (Thermo Fisher Scientific, 17-5941-82), TIM-4 (Thermo Fisher Scientific, 12-5866-82), TIM-4 (BD Bioscience, 742773), CD38 (BioLegend, 102705), F4/80 (Thermo Fisher Scientific, 12-4801-82, 17-4801-80), F4/80 (BioLegend, 123137), LY6C (Thermo Fisher Scientific, 17-5932-80, 25-5932-82), LY6G (Thermo Fisher Scientific, 17-9668-82) and IL-6 (Thermo Fisher Scientific, 12-7061-82) were used for flow cytometry analysis and cell sorting. Absolute number of cells were calculated via Precision Count Beads (BioLegend, 424902). Samples were washed with FACS buffer and resuspended in medium containing 1 μg/mL DAPI. The cells were analyzed using cytoflex LX or BD LSR Fortessa. Cells were sorted using BD Aria III. Data were generated using FlowJo V10 (https://www.flowjo.com/).

To measure intracellular cytokine IL-6, 0.5-5 × 10^6 non-parenchymal cells were incubated for 2-4 h at 37 °C in DMEM with 10% FCS and 1 × brefeldin A (BioLegend). After incubation, cells were stained extracellularly as above. Intracellular cytokine staining was performed by fixing and permeabilizing extracellularly stained cells according to the manufacturer's instructions using the Intracellular Fixation & Permeabilization Buffer (Thermo Fisher Scientific, 88-8824-00). The cells were analyzed using cytoflex LX or BD LSR Fortessa. Data were generated using FlowJo.

To analyze the direct effects of DDC on KCs, freshly isolated KCs from normal livers were treated with DDC at 10 μg/mL or 100 μg/mL *in vitro*. Cells were harvested to analyze the gene expression levels and cell number after 6 hours or 24 hours of incubation.

RNA isolation, qRT-PCR and bulk RNA-seq

Hepatocytes were isolated from mouse livers by a modified two-step liver collagenase perfusion method. Perfused hepatocytes were filtered through a 70 μm filter (BD Bioscience) and were further purified by a series of low-speed gravity centrifugation (50 g × 1 min × 3) as previously described.[72] Total RNA of all hepatocytes was extracted using Trizol (Invitrogen) according to the manufacturer's instructions. The total RNA was quantified and reverse transcribed to obtain the total cDNA. Gene expression was then assayed by quantitative real-time polymerase chain reaction (qRT-PCR) using power SYBR green (Thermo Fisher Scientific) on an ABI StepOnePlus real-time PCR system (Applied Biosystems). Gene expression values were normalized to an internal control of *Gapdh*.

For bulk RNA-seq, sequencing library was prepared from one microgram of total RNA using Illumina TruSeq RNA Sample Prep Kit. Paired-end 150 bp read length sequencing was performed on Illumina Hiseq 4000 sequencer.

To gain transcriptome profiling of immune cells, the low-cell number RNA-seq was applied. Briefly, approximately 20,000 T cells (CD45$^+$CD11b$^-$CD3e$^+$), neutrophils (CD45$^+$CD11b$^+$Ly6G$^+$), macrophages (CD45$^+$CD11b^{lo}Ly6G$^-$F4/80$^+$), monocytes (CD45$^+$CD11b$^+$Ly6G$^-$F4/80$^-$Ly6C^{+or-}) from normal and DDC-injured mouse livers were harvested by FACS. Cell samples were lysed in 50 μL of 4 M guanidine isothiocyanate solution (GuSCN, Invitrogen, 15577-018) at 45 °C for 15 min. Total RNA was precipitated and concentrated by adding 150 μL of nuclease-free water, 600 μL of ethanol, 20 μL of acetate sodium (pH 5.7, 3 M, Ambion) and 1.5 μL of carrier

glycogen (20 mg/mL, Roche). Then total RNA pellets were dissolved in lysis solution and reverse-transcribed and amplified with a modified Smart-seq2 PCR technique, followed by sequencing on Illumina HiSeq 4000. The detailed steps were described previously.[73]

Single-cell RNA-seq

For Smart-seq2 scRNA-seq, a modified Smart-seq2 protocol was applied.[74–76] *Sox9-EGFP* mice were pretreated with DDC injury for 0 day or 7 days. Hepatocytes were purified as previously described.[72] Injured hepatocytes and LPLCs from DDC-injured livers were isolated by sorting GFP^- or GFP^+ hepatocytes by the BD influx cell sorter based on size/granularity and GFP expression. Normal hepatocytes from normal livers were isolated based on size/granularity. After FACS purification, a single hepatocyte was placed into the lysis buffer by the mouth pipette. The reverse transcription reaction was performed with 25 nt oligo (dT) primer anchored with an 8 nt cell-specific barcode and 8 nt unique molecular identifiers (UMI).[77] After the first-strand synthesis, the second-strand cDNA was synthesized, and the cDNA was amplified by 14 cycles of PCR. The amplified cDNA of single cells was then pooled together for the following steps. Biotinylated pre-indexed primers were used to further amplify the PCR product by an additional 4 cycles of PCR to introduce biotin tags to the 3' ends of the amplified cDNAs. Approximately 300 ng cDNA was sheared to approximately 300 bp by Covaris S2, and the 3' terminal of the cDNA was captured by Dynabeads® MyOne Streptavidin C1 beads (Thermo Fisher). The RNA-seq library was constructed using a Kapa Hyper Prep Kit (Kapa Biosystems) and subjected to 150 bp paired-end sequencing on an Illumina HiSeq 4000 platform (sequenced by Annoroad).

For 10X pipeline, isolated hepatocytes or enriched macrophages were processed using the Chromium Single Cell 30 (v3 Chemistry) platform (10X Genomics, Pleasanton, CA). Briefly, for hepatocytes, 10,782 cells from normal livers, DDC-injured livers and macrophage-depleted DDC-injured livers were pooled and sequenced on Novaseq lanes by Novagene AIT. After anti-F4/80 (Ebioscience, 13-4801-82, 1:200) staining and MACS based on anti-Biotin Microbeads (Miltenyi, 130-105-637) using AutoMACS Pro for enriched macrophages, 10,210 non-parenchymal cells from normal livers (*Rosa26-mTmG* mice, for denoting normal liver-derived cells based on *mTomato* expression) and DDC-injured livers were pooled and sequenced on Novaseq lanes by Novagene AIT.

ChIP-seq

Hepatocytes were isolated and purified as previously described.[72] For chromatin immunoprecipitation (ChIP) assay of pSTAT3 in IL-6 induced LPLCs, 1×10^7 cells were cross-linked with 1% formaldehyde for 15 min, followed by glycine quenching for 5 min. After washing in PBS, nuclear extracts were further generated using SimpleChIP® Plus Sonication Chromatin IP Kit (CST, 56383) according to the manufacturer's instructions. For H3K27ac ChIP, E12.5 $DLK1^+$ hepatoblasts, normal-diet mature hepatocytes and $tdTomato^+$ LPLCs from DDC-injured *Sox9-CreERT2;Rosa26-LSL-tdTomato* livers (tracing by intraperitoneal injection of 50 mg/kg tamoxifen) were obtained. Chromatin was fragmented using Q-sonic sonication (20s on, 40s off at total 54 cycles). The following antibodies were used for immunoprecipitation solubilized chromatin: pSTAT3 (CST, 9145, 1:100), H3K27ac (Abcam, ab4729, 1:500) and normal rabbit IgG (CST, 2729P, 1:100) at 4 °C overnight. Antibody chromatin complexes were pulled down with Protein G Dynabeads (Life Technologies, 10004D), washed and eluted. Chromatin cross-links were reversed, and samples were treated with proteinase K and RNase A. Input and ChIP DNA was extracted with the MinElute PCR purification kit (QIAGEN) and quantified with the Qubit (Life Technologies). For ChIP-seq, purified ChIP DNA was used to prepare sequencing libraries via NEBNext Ultra DNA Library Prep Kit for the Illumina (E7370) and sequenced on Illumina Novaseq 6000 sequencer to obtain 150 bp paired-end reads.

Schematics

Schematic cartoons in Figures 4M, 5A, and S6F and Graphical Abstract were created with BioRender.com.

Feature quantification for scRNA-seq data

For 10X dataset, sequencing reads were aligned to the mouse reference genome (mm10) and estimated cell-containing partitions and associated UMI using the Cell Ranger (v6.0.1) single-cell software suite. For Smart-seq2 dataset, nine pair-end libraries, each containing sequencing reads from dozens of single cells, were constructed. For each library, the template switch oligo (TSO) sequences were trimmed by cutadapt (v1.14),[48] and the low-quality bases at 3' end of reads were trimmed by trimmomatic (v0.36).[49] After that, demultiplex was done by fastx toolkit (v0.0.13) (http://hannonlab.cshl.edu/fastx_toolkit). Since we introduced UMI in our Smart-seq2 protocol, we then tagged the UMI sequence to the read name of each sequence by umi_tools.[50] Thus, we got tagged FASTQ files for every assessed cell. As the read2 was mainly composed of polyA sequences, we aligned only read1 of individual FASTQ files to mm10 using STAR aligner (v2.5.2b).[51] Htseq-count (v0.6.0)[52] were used to get UMI count table. Overall, deep sequencing was achieved in our study. For macrophage, the mean total UMI per cell was ~13,600. The mean number of gene detected per cell was 3,412. For hepatocyte, the mean total UMI per cell of 10X and Smart-seq2 data were ~15,000 and ~624,500, respectively. And the mean number of gene detected per cell for 10X and Smart-seq2 data were greater than 2,700 and 8,300, respectively. Saturation analysis of Smart-seq2 data revealed that 100,000 UMI of individual cells were enough to detect over 7,500 genes. For hepatocytes sequenced by 10X Chromium platform, the mean and the median mitochondrial (MT) gene content are 9.85% and 6.94%, respectively. For hepatocytes sequenced by Smart-seq2 platform, the mean and the median MT gene content are 5.41% and 4.72%, respectively. To guarantee the quality of downstream analysis, we only retained hepatocytes with MT gene content less than 10%.

Quality control of scRNA-Seq data

To further acquire more informative datasets, strict criteria were applied to select high-quality cells. The Seurat (v4.0.1)[53,78] R package was employed to perform scRNA-Seq data analysis. For macrophage dataset, cells with total gene detected > 1,500 and mitochondrial (MT) gene content < 5% were selected. For hepatocyte, cells with total UMI > 4,000, number of detected gene > 800, and MT gene proportion < 10% in 10X dataset and cells with total UMI > 100,000 and MT gene content < 10% in Smart-seq2 dataset were selected for the following analysis. After filtering, datasets of different batches were normalized independently with SCTransform. The reciprocal PCA (RPCA)-based integration and graph-based clustering were performed to identify non-hepatocyte contaminants. Cells expressing high level of immune markers (*Cd163*, *Cd68*, *Clec4f*, and *Timd4*) were found in hepatocyte datasets. These were excluded from downstream analysis. To evaluate the effects of liver dissociation to our scRNA-Seq datasets, AddModuleScore function was used to assess the module scores of stress response genes in hepatocytes.[17]

Clustering and trajectory inferring

After quality control, 6,246 and 327 hepatocytes from 10X and Smart-seq2 pipeline left, respectively. For cells sequenced by 10X pipeline, we conducted re-normalization (SCTransform), RPCA-based integration (FindIntegrationAnchors and IntegrateData function), and subsequent clustering (FindClusters with res = 1.5) analysis. The effect of total UMI and MT-gene content were regressed out when normalization. Four-thousand most variable genes were used for analysis. Uniform manifold approximation and projection (UMAP) is used for visualization. Cellular trajectory was constructed using monocle3 (v1.0.0)[54,79] R package. To ensure consistency between hepatocyte subpopulations and cellular trajectory, we conducted pseudo-temporal analysis in a semi-supervised manner that the principal component (PC) values generated from Seurat integrated dataset were used as the input of 'reduce_dimension' function in monocle3. To validate the cellular subpopulations and trajectory found in 10X dataset, Smart-seq2 data containing cells assessed in two batches was analyzed independently using the same pipeline descripted above.

Identification of hepatocytes subpopulations

To increase the power, the 10X libraries were prepared pooling normal and DDC-diet hepatocytes together. To distinguish them, a public dataset (GSE125688)[40] and our Smart-seq2 dataset in which the normal and DDC-diet hepatocytes were assessed separately were used. The normal and DDC signature genes were identified as DEGs ($|\log_2 FC| > 1.5$, adjusted P value < 0.05) between two conditions. Genes with high expression level in the opposite condition (rank of median expression level <= 500) were removed from signature. AddModuleScore function was used to score these two signatures of all cells in 10X datasets. By subtracting DDC signature score from normal signatures, we got N-score for each cell. Cells with N-score greater than 0 were regarded as normal hepatocytes. For DDC-diet cells (Figure 1C), FindAllMarkers function was used to calculate the feature genes of each cluster. Clusters were grouped into subpopulations according to the expression pattern of feature genes (Figure S1E). These subpopulations were annotated according to feature gene, pseudotime, and locations on cellular trajectory.

Identification of RRGs

As the hepatic reprogramming goes from normal hepatocytes to injured hepatocytes and finally LPLCs, two types of gene were considered significantly associated with this process: (1) significantly upregulated in LPLCs ($\log_2 FC > 0.35$, adjusted P value < 0.05) compared to both normal hepatocytes and injured hepatocytes; (2) exclusively expressed in LPLCs ($\log_2 FC > 0.35$, adjusted P value < 0.05, percentage of LPLCs expressing corresponding gene > 0.25, and percentage of non-LPLCs expressing corresponding genes < 0.1). To further decrease the false positive rate, bulk RNA-Seq samples of enriched normal hepatocytes and LPLCs were also used. Genes with high expression level ($\log_2 FPKM >= 6$) in normal hepatocytes were removed. For the rest genes, those with $\log_2$(LPLCs/normal hepatocytes) > 0.5 in bulk RNA-Seq samples were retained. For the full list of RRGs, please refer to Table S1. To evaluate whether *Sox9* and RRGs were activated in APAP-induced liver injury, the processed Seurat R object was downloaded from a previously published study.[39] And the module scores of RRGs for individual hepatocytes were assessed by AddModuleScore function.

scRNA-Seq data analysis of immune cells

After normalization, 3,000 MVGs were selected. Principle component analysis was conducted based on the scaled expression level of MVGs. Robust PCs (PC1 to 15) were identified and used for further dimension reduction and neighbor detection. Clustering was conducted using FindClusters function with resolution set to 0.5. Cells of different clusters were annotated according to expression of marker genes. Mann–Whitney U tests were used to identify differential expressed cytokines among immune cell populations. The list of mouse cytokines was collected from UniProt (https://www.uniprot.org). To delineate the heterogeneity of DDC-treated Kupffer cells, they were extracted, re-normalized, and re-clustered. For the full list of feature genes and enriched pathways of two subpopulations in DDC_KC, please refer to Table S3.

Pseudotime-based pathway activity analysis

To unravel pathway dynamics along hepatocyte reprogramming, we assessed single-cell pathway activity by calculating normalized enrichment score (NES) on Reactome pathway (https://reactome.org) using GSVA R package (v1.38.2).[56] Log-scaled SCTransform-normalized UMI matrix was provided to gsva function. The limma R package (v3.46.0)[57] was used to perform pairwise comparisons of NES values between cell subpopulations. Pathways that showed significant changes ($|\log_2 FC| > 0.1$ and FDR adjusted P value < 0.05)

between any two subpopulations were selected. And un-supervised hierarchical clustering was performed (pheatmap R package v1.0.12) to these pathways to decipher their changing patterns along hepatocyte reprogramming. Given the highly noised nature of scRNA-seq data, we performed de-noising processing before clustering. For each selected pathway, we fitted a smooth curve between NES values and pseudotime (loess fit, span = 0.75). The de-noised NES values were calculated as predicted NES values against original pseudotime. Given that cells under same state were likely assigned similar pseudotime, we divided the whole time to 0.05 size long time bins. For each time bin, the corresponding pathway activity was calculated as the mean de-noised NES values of all cells within the bin. Thus, the smoothed NES table, whose row represent pathways, columns represent time bins, was used for clustering analysis. The smoothed NES table that generates Figure 1H was provided as Table S2.

Bulk RNA-seq data analysis

The sequencing reads were mapped to the mm10 using STAR algorithm. Htseq-count algorithm was used to count reads mapped to each gene uniquely. DESeq2[58] R package was used to detect differentially expressed genes (DEGs) between groups. ClusterProfiler (v3.18.1)[59] R package was used to perform enrichment analysis of gene sets to Reactome pathway. Gene Set Enrichment Analysis (GSEA)[55] was employed to detect gene sets that exhibited significant differences between given groups. Heatmaps that represent gene expression pattern across groups were generated with pheamap.

ChIP-seq data analysis

All trimmed sequencing reads were aligned to Mm10 (mouse genome) by using Bowtie2.[60] Peak calling was identified using MACS v2.1.1[61] with the q-value cut-off of 0.05. Biological replicates showed high degree of similarity so the replicate data were subsequently combined and processed. Heatmap and signal tracks of STAT3 and H3K27ac were presented by deepTools v2.5.3[62] and Integrative Genomics Viewer (IGV) software.[63] For identification of STAT3 and H3K27ac peaks in reprogramming-related genes, nearby cis-elements were identified via GREAT.[64]

ATAC-seq data analysis

ATAC-seq data of *Arid1a-WT* hepatocytes, *Arid1a-KO* hepatocytes and LPLCs were retrieved from published ATAC-seq data (GSE111502). Sequence aligning, peaks calling, and visualization were generated as described for CHIP-seq data analysis.

QUANTIFICATION AND STATISTICAL ANALYSIS

All experimental data were presented as the mean ± SD. ‘‘n’’ represented the number of animals and was indicated in the Figures and Figure legends. For quantification of liver sections, three to five random periportal fields of each liver samples unless otherwise specified were imaged and then quantified using Image J or QuPath v0.2.3. No statistical method was used to predetermine sample size. All siblings with indicated genotypes were randomly used in this study. Sample processing was not blinded. For statistic evaluation, an unpaired two-sided Student’s t-test was performed using Graphpad Prism 8 software and mentioned in the Figure legends.